ISSN: 2153-1196 Volume 13, Number 9, September 2022

Scientific Research Publishing

Journal of Modern Physics

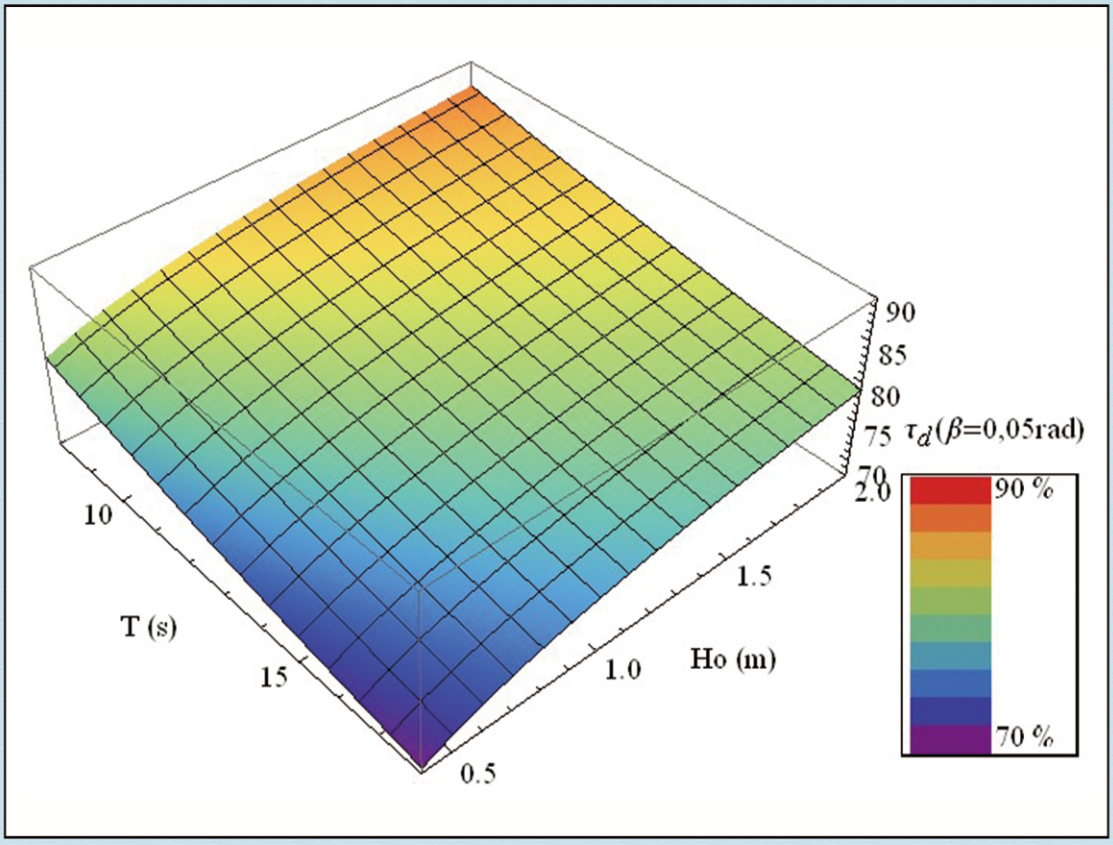

ISSN: 2153-1196

https://www.scirp.org/journal/jmp

Journal Editorial Board

ISSN: 2153-1196 (Print) ISSN: 2153-120X (Online)
https://www.scirp.org/journal/jmp

Editor-in-Chief

Editorial Board

Journal of Modern Physics, 2022, 13, 1253-1294
https://www.scirp.org/journal/jmp
ISSN Online: 2153-120X
ISSN Print: 2153-1196

Table of Contents

Volume 13 Number 9 September 2022

The figure on the front cover is from the article published in Journal of Modern Physics, 2022, Vol. 13, No. 9, pp. 1272-1286 by Oswald G. Acclassato *et al.*

Journal of Modern Physics (JMP)
Journal Information

SUBSCRIPTIONS

The *Journal of Modern Physics* (Online at Scientific Research Publishing, https://www.scirp.org/) is published monthly by Scientific Research Publishing, Inc., USA.

Subscription rates:
Print: $89 per issue.
To subscribe, please contact Journals Subscriptions Department, E-mail: sub@scirp.org

SERVICES

Advertisements
Advertisement Sales Department, E-mail: service@scirp.org

Reprints (minimum quantity 100 copies)
Reprints Co-ordinator, Scientific Research Publishing, Inc., USA.
E-mail: sub@scirp.org

COPYRIGHT

PRODUCTION INFORMATION

For manuscripts that have been accepted for publication, please contact:
E-mail: jmp@scirp.org

Scientific Research Publishing

Journal of Modern Physics, 2022, 13, 1253-1266
https://www.scirp.org/journal/jmp
ISSN Online: 2153-120X
ISSN Print: 2153-1196

Proposal of a Model of a Three-Dimensional Spherical Universe

Hitoshi Shibata[1], Norio Ogata[2*]

[1]Taiko Pharmaceutical Company, Limited, Osaka, Japan
[2]R & D Department, Taiko Pharmaceutical Company, Limited, Kyoto, Japan
Email: *nogata7@yahoo.co.jp

How to cite this paper: Shibata, H. and Ogata, N. (2022) Proposal of a Model of a Three-Dimensional Spherical Universe. *Journal of Modern Physics*, **13**, 1253-1266.
https://doi.org/10.4236/jmp.2022.139074

Received: July 18, 2022
Accepted: August 28, 2022
Published: August 31, 2022

Abstract

Despite the existence of several exact solutions to the general theory of relativity, it is still difficult to explain the entire structure of the universe. In this paper, we propose a novel three-dimensional spherical (S^3) universe model. According to this model, the universe had a powerful gravity source at its origin, and a part of the gravitational source formed a bubble of spacetime in which the universe was born. The universe expanded explosively immediately after the Big Bang. The energy obtained from the gravity source at the birth of the universe is constant, that is, it remains constant from the birth of the universe to the end. The expansion and contraction of the universe is determined by the passage of coordinate time. The S^3 universe observed from outside can be considered to be a two-dimensional spherical surface by projecting it onto a three-dimensional space. On the other hand, the visible universe viewed from inside is observed as a three-dimensional sphere with an arbitrary observation point. The origin of the S^3 universe can be seen to be evenly spread in the outer shell of the visible universe. We define *visible longitude* as the difference between an observation point and its farthest light source. At an initial phase of the expansion of the universe, few stars can be seen, because the visible longitude is small. However, when the expansion of the universe progresses, the number of visible stars also increases, since visible longitude increases. In our S^3 universe model, the redshifts observed and reported so far in literature appear to indicate that the expansion of the universe is accelerating. Our S^3 universe model can thus lead to a novel exact solution to general relativity.

Keywords

Redshift, S^3 Universe, Expansion, General Relativity, Big Bang

1. Introduction

Current exact solutions to general relativity can correctly explain the deforma-

tion of spacetime under specific conditions [1] [2] [3] [4] [5], but Freedman's solution, which explains the chronological changes of the entire universe, cannot explain the accelerated expansion of the universe [6] [7] [8]. We present in this paper a three-dimensional spherical (S^3) universe model. This model can show the entire structure of the universe as seen from outside of the universe from its birth to its end, as well as the chronological changes of the universe as observed from inside. The S^3 universe has a strong source of gravity in its center, and a part or all of it became a spacetime bubble where the universe was born [9]. The S^3 universe was explosively expanded by the Big Bang shortly after its birth, just like the current universe [9], eventually becoming a great sphere after the rate of expansion had slowed. Soon after, the S^3 universe started to contract gradually; the speed of the contraction increased until it finally contracted to the original origin (**Figure 1**) [9] [10].

When the S^3 universe is viewed from outside, it is possible to define the chronological changes of the entire structure using coordinate time, which can express the expansion and contraction of the S^3 universe. On the other hand, when viewed from inside, the S^3 universe appears, similar to the current universe, as a celestial sphere that spreads evenly in all directions [11] [12]. Soon after the birth of the S^3 universe, light reaching an arbitrary observation point is only the nearest light of the Big Bang. After the birth of stars, the light from neighboring stars reaches sequentially, and when the expansion speed of the S^3 universe slows

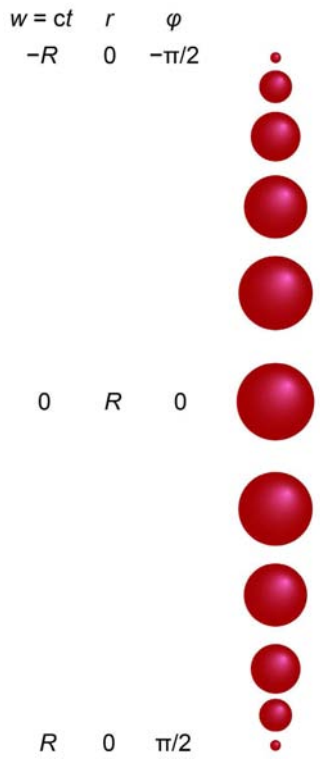

Figure 1. Life of the S^3 universe. The red spheres show the expansion and contraction of the S^3 universe with the passage of coordinate time from an external view. r represents the radius at coordinate time $w = ct$, and φ represents the latitude of the S^3 universe.

down, light from a long distance away starts to arrive sequentially. The longitude difference between the farthest light source from which light can be emitted and the observation point is defined as *visible longitude*. Stars visible in the entire celestial sphere are sparse at the beginning of the expansion since the visible longitude is small then, but the number of visible stars increases as the universe expands as a result of the increase in visible longitude. When the universe reaches its maximum expansion, the light from the observation point reaches the visible longitude of π/2. The visible longitude increases even during the contraction phase, as does the number of visible stars. Finally, the universe contracts to the origin and ends when the contraction speed increases and cosmic microwave background (CMB) reaches the longitude difference of π [9]. From the standpoint of an internal view of the universe, the gravity source, which is the origin of the universe, is in the outer shell of the celestial sphere, and the entire universe can be interpreted to be the bubble of spacetime floating in the gravity source at the origin [9].

2. Definition of the S^3 Space Model

The S^3 universe is represented by four dimensions: x, y, and z-coordinates for space, and the w-coordinate that indicates space expansion and contraction. The w coordinate has a dimension of distance determined by multiplying time t by the speed of light c, where t is defined as the coordinate time of the S^3 universe. When the radius of the great sphere of S^3 at coordinate time zero is R, the relationship $x^2 + y^2 + z^2 + w^2 = R^2$ holds. When the radius of the S^3 universe at coordinate time t ($w = ct$) is r, the latitude of the S^3 is defined as φ as shown in **Figure 1** and **Figure 2**. Latitude φ is zero on the great sphere ($w = 0$) and $\varphi = \arcsin(ct/R)$ at arbitrary coordinate time t ($w = ct$), where $-\pi/2 \le \varphi \le \pi/2$. The rate of increase of the radius r at coordinate time t is defined as the expansion speed of the S^3 universe, which is expressed by v. They are related by the expressions $r = R\cos(\varphi)$ and $v = dr/dt = -c\tan(\varphi)$. As shown by the green line in **Figure 2**, the radius r of the S^3 universe becomes zero at a start point ($w = -R$), R at the great sphere ($w = 0$), and zero again at an end point ($w = R$). On the other hand, as shown by the blue line in the figure, the expansion speed v of the radius r is maximum immediately after the start point, zero on the great spherical surface, and negative maximum just before the end point.

In this paper, without considering local spacetime distortions, we believe that the expansion and contraction of the S^3 universe occur evenly in all directions of the space coordinates, and that the celestial bodies in the S^3 universe are stationary at each respective position. Therefore, even if the radius of the S^3 universe changes, the relative positions of the celestial bodies in the space coordinates do not change. As shown in **Figure 3**, the angle β formed by the directions of the expansion velocity vectors of the two celestial bodies represents the longitude difference between the two celestial bodies, and this longitude difference is always constant regardless of the expansion and contraction of the S^3 universe.

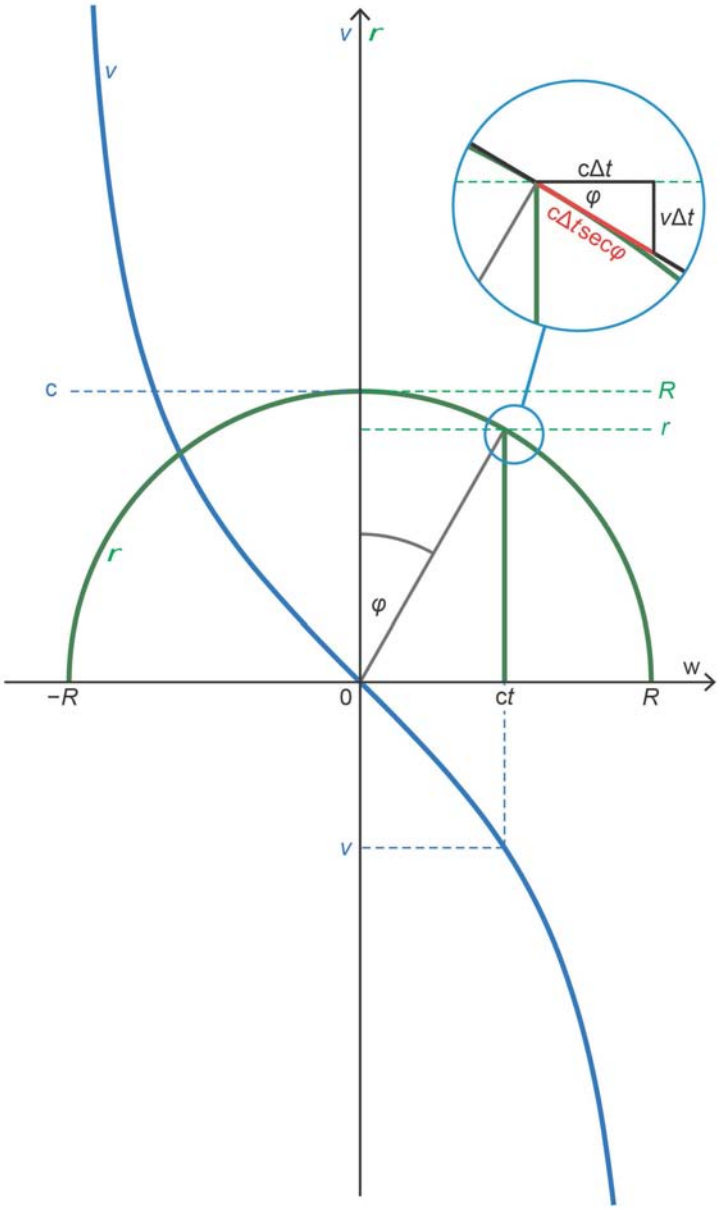

Figure 2. Radius of the S^3 universe and its expansion velocity. The green semicircle shows the change in the radius r of the S^3 universe with the passage of $w = ct$ at the coordinate time. φ is the S^3 latitude of the radius r at $w = ct$ with respect to the great sphere at $w = 0$. The blue curve depicts the expansion speed v of the radius r. In the enlarged circled inset, the ratio of the elongation $v\Delta t$ of the radius r to the advancement $c\Delta t$ of coordinate time is shown to be the same as the expansion speed ratio $v/c = -\tan(\varphi)$ with respect to the speed of light at latitude φ. Since this figure shows a contraction process, v is negative.

3. A Light Path of the S^3 Universe

For a stationary light source and observation point, the light path (distance of geodesic) that runs in the S^3 universe is elongated when compared to the light path that runs in a stationary space, because the radius r of the S^3 universe changes during the time it takes for the light emitted from the light source to reach the observation point. As shown in Figure 2 (circled), the light path of a

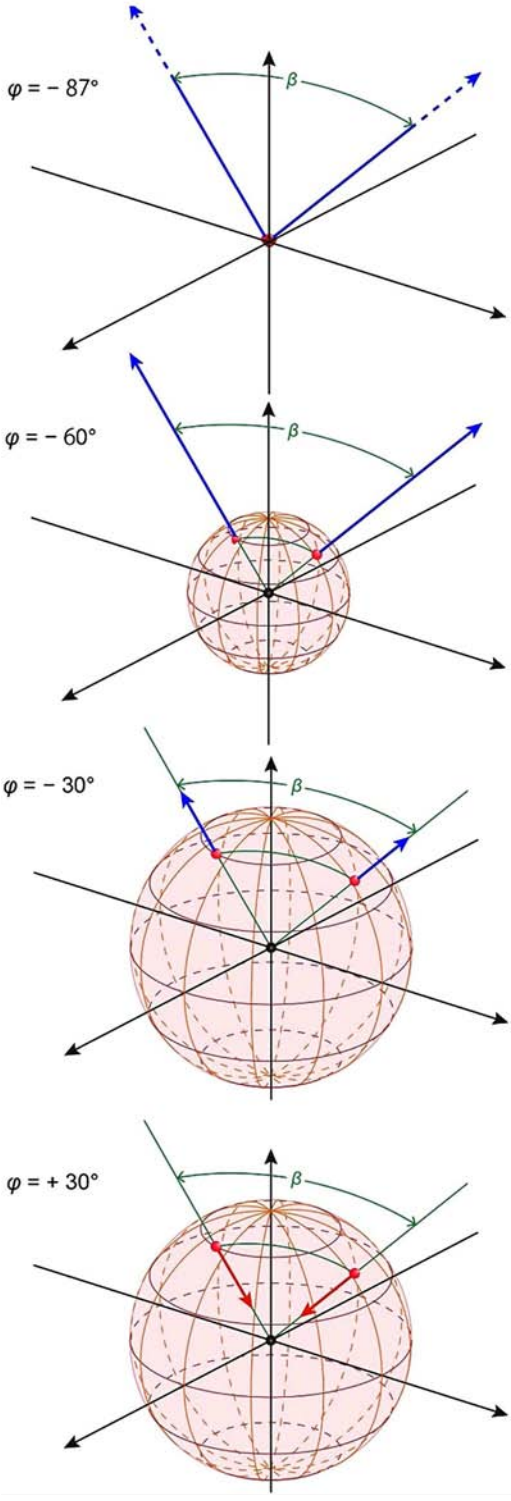

Figure 3. Longitude difference between two celestial bodies. This represents the S^3 universe at each latitude φ as seen from the outside. The small red spheres represent both stationary celestial bodies, and the arrows extending from the celestial bodies represent positive expansion velocity vectors in blue and negative expansion velocity vectors in red, respectively. The angle β formed by the expansion velocity vectors of the two celestial bodies is the longitude difference between their spatial coordinates, and it is always constant regardless of the latitude φ of the S^3 universe.

minute distance is elongated to the distance of hypotenuse $c\Delta t\sec(\varphi)$ compared to the distance $c\Delta t$, when light runs in a stationary space. This elongation of the light path occurs due to the principle of constant light speed. The reason for this is that the proper time needed for the light to travel this minute distance is greater than the coordinate time required to travel the same distance. When the proper time of the S^3 universe at latitude φ is τ, the light path of the minute distance, $c\Delta\tau \approx c\Delta t\sec(\varphi)$, and the elongation of the proper time relative to the coordinate time can be expressed as $d\tau/dt = \sec(\varphi)$, as shown in Figure 4 (blue line). When the ratio $\sec(\varphi)$ is integrated so that the proper time begins from zero and the integration constant is $\pi/2$, the following equation that shows the elongation of the proper time with respect to coordinate time is obtained as shown in Figure 4 (green line).

$$\alpha = \frac{c}{R}\int \sec(\varphi)\,dt = \frac{c}{R}\int\left[\arcsin\left(\frac{ct}{R}\right)\right]dt = \arcsin\left(\frac{ct}{R}\right)+\frac{\pi}{2} = \varphi+\frac{\pi}{2} \qquad (1)$$

The result of this integration shows the advancement of longitude (angular distance), in which light runs in the expanding or contracting space coordinate from the origin, while coordinate time advances in the direction of the w-coordinate

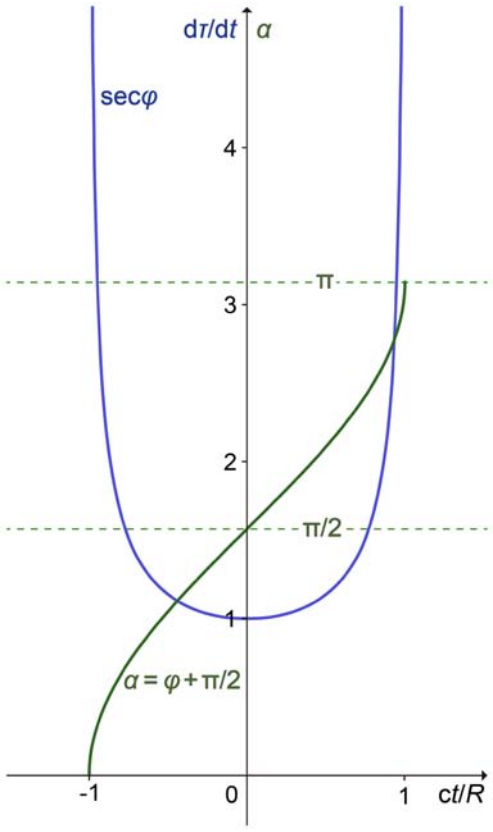

Figure 4. Progression of proper time and visible longitude of the S^3 universe. The horizontal axis represents the ratio of the w-coordinate to the maximum radius R. The blue line shows the progression of the proper time with respect to the coordinate time $d\tau/dt$. The green line depicts the angular distance α traveled by the light of the Big Bang, which is the visible longitude of the observable universe.

from $w = -R$ to ct. Since this is what we call visible longitude α, the equation of $\alpha = \varphi + \pi/2$ holds true. The path of light in the S^3 universe from origin to latitude φ is shown by a green arc of radius $R/2$ in Figure 5(d), and the distance of the light path is the same as the arc of the great circle Ra of radius R and angle α depicted in Figure 5. This Ra represents the optical path length of the Big Bang light, namely the CMB observed at an arbitrary latitude φ, and Ra is hereinafter referred to as an optical radius. In Figure 5, the longitude difference between the observation point G and the light sources G_0, G_1, G_2, and G_3 on the optical path is always constant. Therefore, the longitude difference β between the observation point and each light source is equal to the difference between latitude φ when the light is observed at the observation point and latitude φ_s when the light is emitted from the light source. In other words, $\beta = \varphi - \varphi_s$ holds.

4. Structure of the S^3 Universe as Revealed by an Internal View

We consider a single path of light from the Big Bang that ran soon after the birth of the S^3 universe. When this light travels on an S^3 circumference with varying radius r and arrives at an observation point, it appears to an observer to be travelling in a one-dimensional straight line. This one-dimensional straight line is a line segment of a certain length for an observer standing in the center. The distance from the observer to the end of the line segment is optical radius a of the light from the Big Bang. The observer observes the light simultaneously with light emitted on the same line by a star. Here we assume a three-dimensional space in which all lights appear straight, and we use Cartesian coordinates x', y', z' with an observation point G as an origin. Two paths of light are emitted at the Big Bang and reach the observation point by running right and left on the circumference of the S^3 universe becoming one-dimensional segments starting from an origin G and extending right and left on the x'-axis of these coordinates, as shown in Figure 6(a). When this line is rotated 180 degrees (π) around the z'-axis, it becomes an inside-filled circle of radius Ra in a two-dimensional x-y plane, as shown in Figure 6(b). Lights coming from all directions to an observer in the center include not only the lights from the Big Bang, but also lights originating in stars and traveling along the light paths. Furthermore, when the two-dimensional circle is rotated 180 degrees (π) around the y-axis, it generates an inside-filled three-dimensional sphere of optical radius Ra at the time of observation, as shown in Figure 6(c). This sphere represents the visible universe at latitude φ, and the origin of the S^3 universe appears evenly spread in the outer shell of the visible universe at that time. We show the changes in latitude φ and optical radius Ra of the visible universe with the passage of coordinate time in Figure 7(a) and Figure 7(b). The rate of change of the optical radius of the visible universe is shown by the blue line in Figure 4 and is the same as the change of $\mathrm{d}\pi/\mathrm{d}t$; it decreases during an expansion phase and increases during a contraction phase. When the farthest light (electromagnetic wave) from visible longitude π reaches the observation point, the entire universe converges to one point and ends.

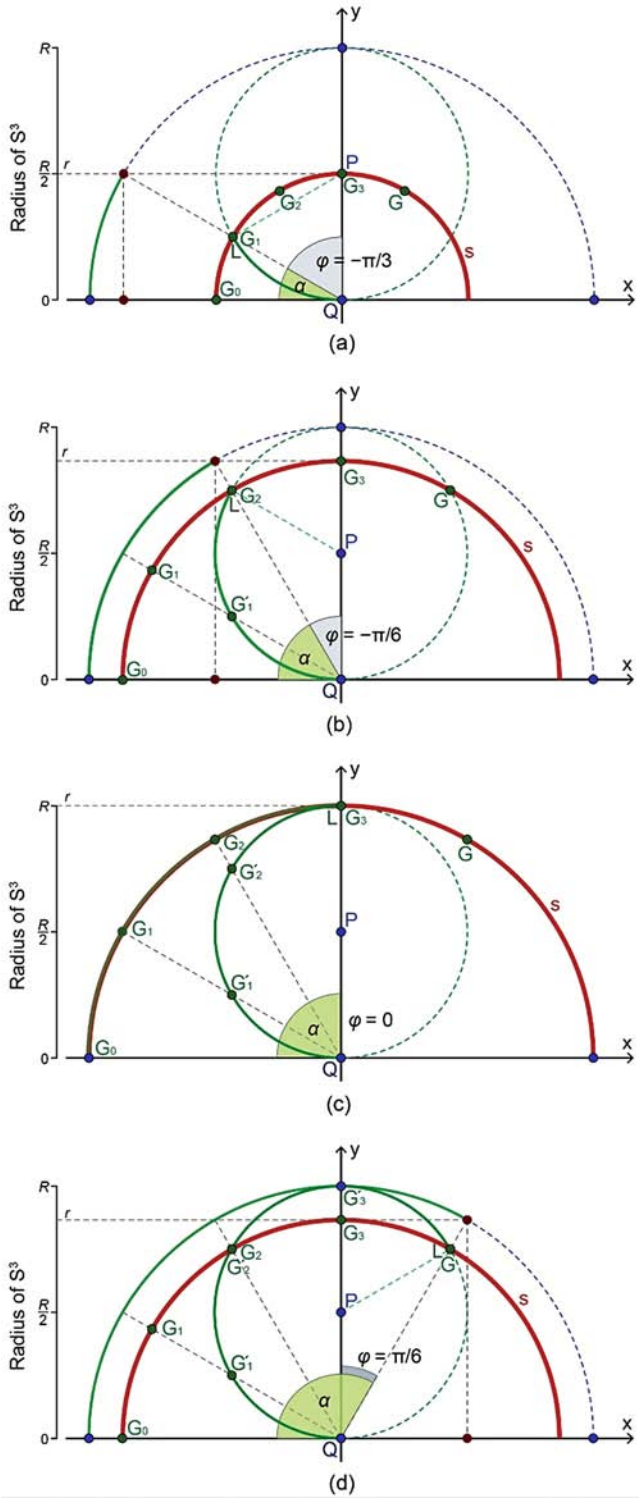

Figure 5. The red semicircles in panels (a), (b), (c) and (d) show x-y cross sections of the S^3 universe at latitude φ, and the green arc QL of radius $R/2$ and center P shows a path of light emitted from origin Q and running the distances of $\alpha = \pi/6$, $\pi/3$, $\pi/2$ and $2\pi/3$, respectively. The light path of arc QL is the same as the length Ra of the arc EM, which is a projection of radius R on the great sphere. G_0, G_1, G_2, G_3 and G are celestial bodies on the light path, and longitude differences between them do not change despite the changes in the radius of the S^3 universe.

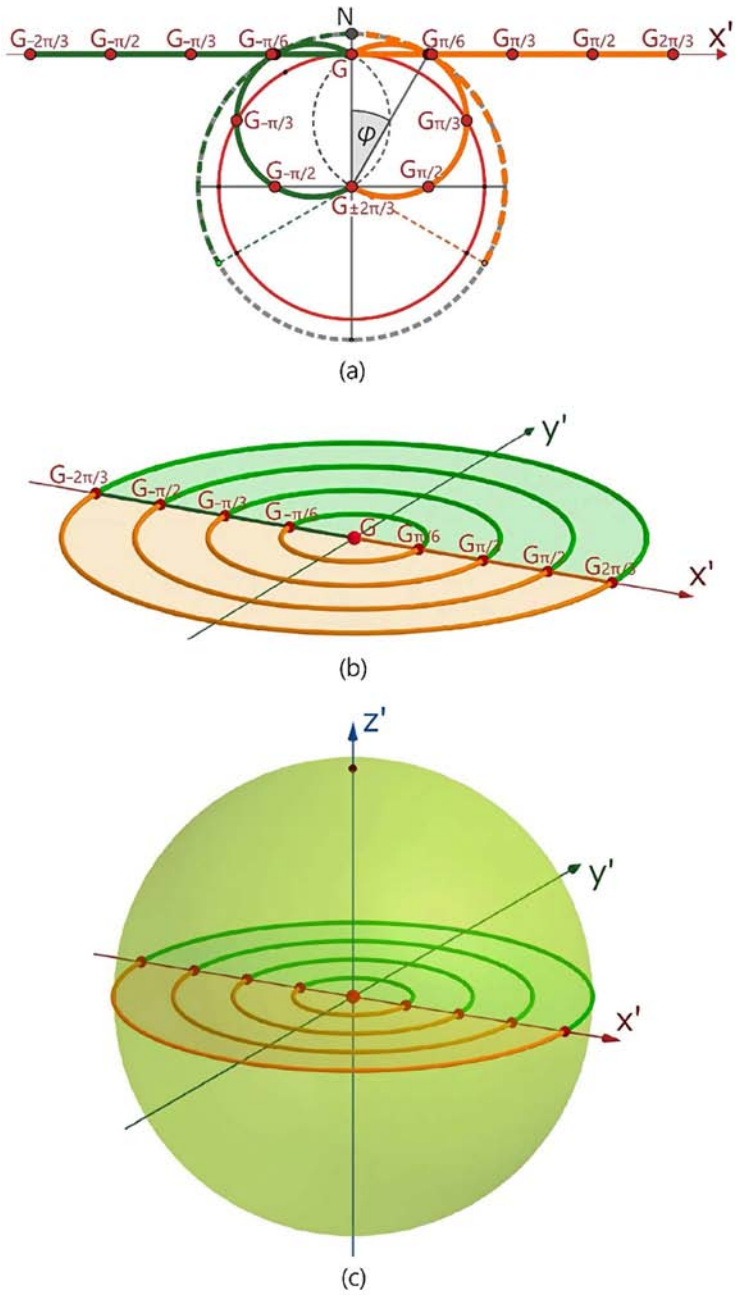

Figure 6. Visible structure of the S^3 universe. (a) The red circle is the circumference s at latitude $\varphi = \pi/6$, and G is the stationary observation point on the circumference. The green and orange arcs indicate optical paths (light trajectories) from the visible longitude $\pm\alpha$ ($\alpha = \varphi + \pi/2 = 2\pi/3$) observed at point G at $\varphi = \pi/6$. Gs with a subscript indicate the optical path positions of a light source (an astronomical object) at the time of emission. Each subscript represents the longitude β from observation point G. The horizontal green and orange lines extending from G to the left and right are line segments on an x'-coordinate axis of three-dimensional Cartesian coordinates (x'-, y'-, z'-axis) with observation point G as the origin. The optical radius ($R\alpha = 2\pi R/3$) is given from the observation point G to the left and right. (b) When this one-dimensional line segment is rotated through 180 degrees (π), it becomes a two-dimensional circle with radius a on the x-y plane. (c) When this two-dimensional circle is rotated 180 degrees (π), it transforms into a three-dimensional sphere with an optical radius *Ra*.

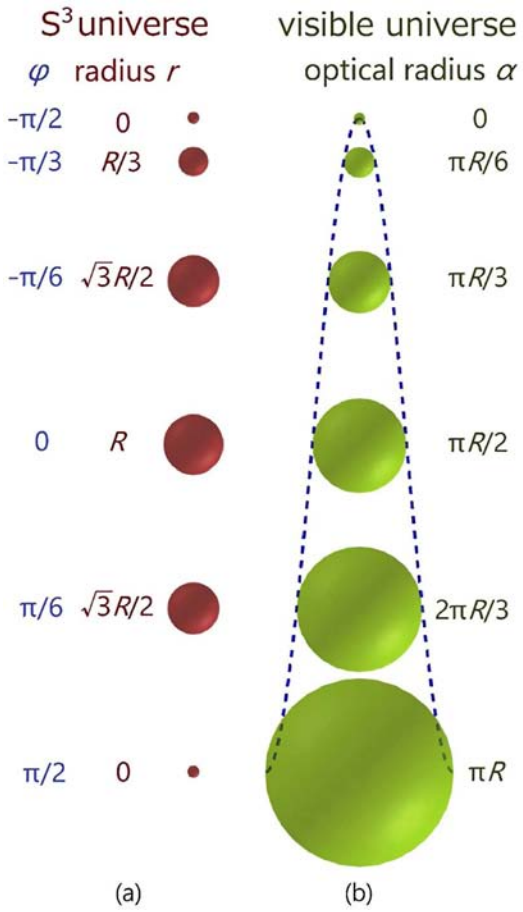

Figure 7. The S^3 universe as seen from external and internal perspectives. (a) The red spheres show the S^3 universe as seen from the outside at some latitude φ. (b) Yellow-green spheres are full three-dimensional spheres that represent the visible universe with an optical radius a that can be observed from any point G inside the S^3 at latitude φ.

5. Redshift Observed in the S^3 Universe

The observation that the current universe appears to be expanding in an accelerated way [13] [14] [15] [16] is also confirmed in our S^3 universe model. The reason for this observation is that we are looking at past light emitted by a star when the velocity of expansion was larger than that at the time of observation. According to the principle of constant light velocity, we believe that light in a flat spacetime travels at velocity c with respect to the coordinate time t, and light in an expanding or contracting S^3 universe travels at velocity of c with respect to the proper time τ of a passing point. Consequently, the expansion velocity of the radius r against the light velocity $v/c = -\tan(\varphi)$ can be regarded as elongation of proper time τ at latitude φ against coordinate time t. During the expansion phase of the universe, the rate of expansion decreases depending on the light path, namely the difference in longitude, during the period of light emission to the observation point with the passage of time (the area of positive v in Figure 2). Therefore, redshift increases, as the passage of proper time at the time of observation is delayed compared to that at light emission, and the wave length of

the observed light increases. Since the energy of light at the time of emission reflects the frequency determined by the proper time, and the increase of proper time compared to coordinate time at the time of emission at latitude φ is $\sec(\varphi)$ (blue line in Figure 4), the frequency ν_τ of light L at the emission time in terms of proper time becomes $\sec(\varphi)$-fold of the frequency ν_t of coordinate time. In other words, $\nu_\tau/\nu_t = \sec(\varphi)$, and the ratio of wave lengths becomes the inverse of this equation, namely, $\lambda_\tau/\lambda_t = \cos(\varphi)$.

When the observation point G is on the S^3 universe of latitude φ, we consider the light that has travelled a distance of $R\beta$ from the light source G_s to an observation point G with longitude difference β. If we assume that a light source G_s at the time of light emission is of latitude φ_s, the wave length of the light in terms of proper time at the time of emission is λ_s, the latitude of the observation point G at the time of observation is φ and the wave length in terms of proper time is λ. We obtain $\varphi_s = \varphi - \beta$, because the longitude difference β between the observation point and the light source is the same as the latitude difference $\varphi - \varphi_s$ between the times of light emission and observation. If the elongation of the wave lengths of a light source and an observation point, in terms of proper time are respectively $\lambda_s/\lambda_t = \cos(\varphi_s)$ and $\lambda/\lambda_t = \cos(\varphi)$, the elongation of the wave length at the time of observation against that of emission is expressed as follows.

$$\frac{\lambda}{\lambda_s} = \frac{\lambda/\lambda_t}{\lambda_s/\lambda_t} = \frac{\cos(\varphi)}{\cos(\varphi_s)} = \frac{\cos(\varphi)}{\cos(\varphi-\beta)} \tag{2}$$

An uppercase letter Z is used to denote the redshift to distinguish it from the letter z for coordinate. When the above equation is inserted in the redshift equation $Z = \lambda/\lambda_s - 1$, the following equation that shows redshift in the S^3 universe is obtained.

$$Z = \frac{\cos(\varphi)}{\cos(\varphi-\beta)} - 1 \tag{3}$$

Figure 8 shows a relationship between the longitude difference β from the observation point to the light source and redshift by selecting latitudes of the observation points of the S^3 universe at regular intervals. It can be understood from this figure that the redshift increases in an accelerated fashion as the longitude difference β between the light source and the observation point increases, and the curve of increase becomes milder with the increase in φ of the observation point. On the other hand, during the contraction phase ($\varphi > 0$), blueshift starts to appear, with minus Z beginning from the light of small β and the light source to large β in this order. Upon the increase in latitude φ, the area of the blueshift expands. At the observation point during the contraction phase, blueshift increases when the longitude difference is $\beta < \varphi$, since Z becomes minus; blueshift becomes maximum at $\beta = \varphi$, and the next blueshift decreases at $\varphi < \beta < 2\varphi$, and finally $Z = 0$ at $\beta = 2\varphi$. Furthermore, we found that the redshift Z increases in an accelerated fashion even during the contraction phase, depending on the increase in longitude difference β, when the longitude difference β exceeds

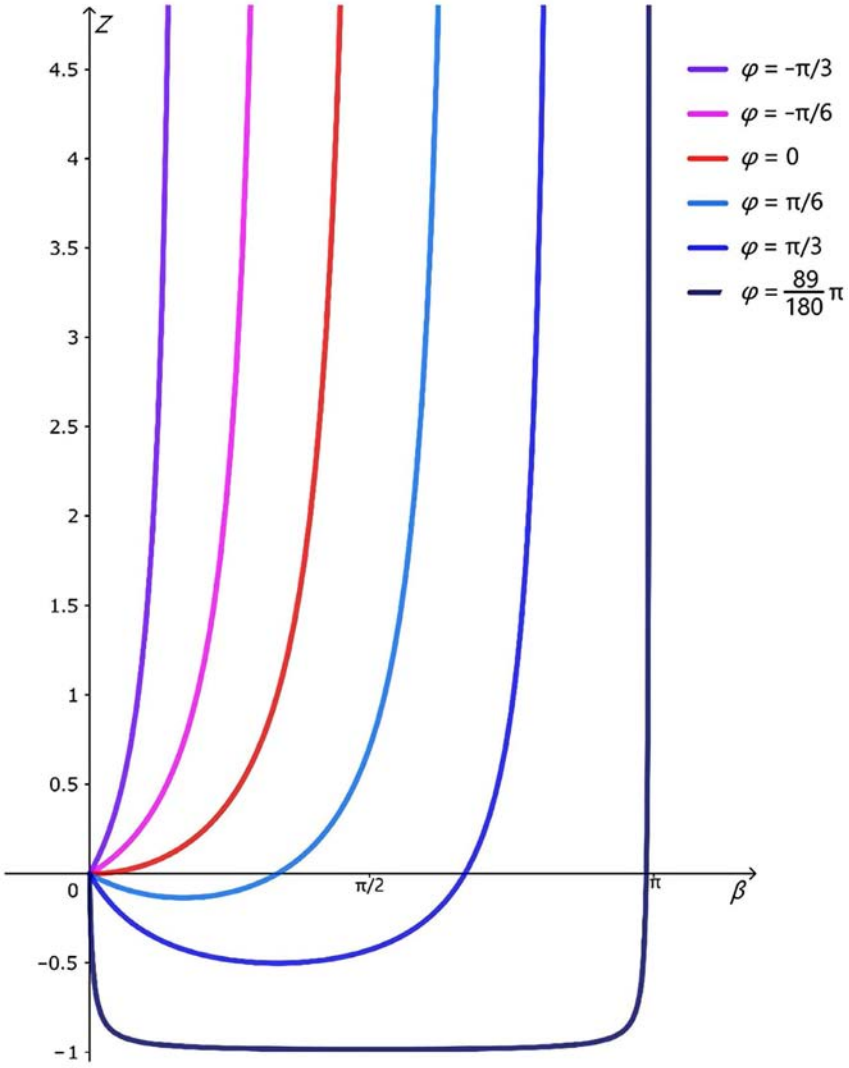

Figure 8. Redshift in the S^3 universe. This figure shows redshift of light observed at latitudes $\varphi = -\pi/3, -\pi/6, 0, \pi/6, \pi/3$ and $(89/180)\,\pi$. The vertical axis represents redshift Z, and the horizontal axis depicts the difference in longitude β between the observation point and the light source.

2φ. We also discovered that the redshift Z at the observation point of latitude φ is determined by the light path $R\beta$ up to the light source, because the horizontal axis β of Figure 8, namely the difference β, is proportional to the length of the light path $R\beta$.

6. Conclusion

In our S^3 universe model, the visible universe is seen from the internal viewpoint as a three-dimensional sphere centered on an arbitrary observation point G, and the origin of the S^3 universe appears to spread evenly over the entire celestial body, which is the outer shell of the visible universe. The longitude difference between stationary celestial bodies in the S^3 universe is always constant, and the optical path length of light emitted from the celestial body of the light source

and reaching the celestial body of the observation point is always constant, regardless of the change in the dynamic diameter of the S^3 universe. However, as shown in **Figure 8**, the redshift observed in the S^3 universe is determined by the longitude difference β between the light source and the observation point, as well as the latitude φ of the S^3 universe at the time of observation. From the internal viewpoint of the S^3 universe, when the universe expands and reaches the large spherical surface and then contracts, the blueshift is observed in the order from the celestial body with the smallest longitude difference (**Figure 8**, $\varphi = \pi/6$ blue curve, and $\pi/3$ dark blue curves). On the other hand, blueshifts have been observed in some of the closest galaxies in the present universe, which in the S^3 universe model coincides with the early stage of contraction immediately after the large sphere. Furthermore, from the observation of type Ia supernovae, it seems that the current universe began to accelerate and expand again, which is consistent with the increase in negative expansion rate in the early stages of the contraction of the S^3 universe. This result suggests that the S^3 universe model is one of the leading candidates for the temporal change in the geometry of the present universe.

Conflicts of Interest

The authors declare no conflicts of interest regarding the publication of this paper.

References

[1] Durgapal, M.C. (1982) *Journal of Physics A*: *Mathematical and General*, **15**, Article No. 2637. https://iopscience.iop.org/article/10.1088/0305-4470/15/8/039/meta https://doi.org/10.1088/0305-4470/15/8/039

[2] Pant, N., Fuloria, P. and Tewari, B.C. (2012) *Astrophysics and Space Science*, **340**, 407-412. https://doi.org/10.1007/s10509-012-1068-8

[3] Murad, M.H. and Fatema, S. (2012) *Astrophysics and Space Science*, **343**, 587-597. https://doi.org/10.1007/s10509-012-1277-1

[4] Momeni, D. and Miraghaei, H. (2009) *International Journal of Modern Physics A*, **24**, 5991-6000. https://doi.org/10.1142/S0217751X09046369

[5] Liu, H. and Wesson, P.S. (1992) *Journal of Mathematical Physics*, **33**, 3888-3891. https://doi.org/10.1063/1.529835

[6] Wendy, W.L., Michael, S. and Turner, M.S. (2003) *Reviews of Modern Physics*, **75**, 1433-1447. https://doi.org/10.1103/RevModPhys.75.1433

[7] Freedman, W.L. (2017) *Nature Astronomy*, **1**, Article No. 0121. https://doi.org/10.1038/s41550-017-0121

[8] Spergel, D.N., Bolte, M. and Freedman, W. (1997) *Proceeding of the National Academy of Science USA*, **94**, 6579-6584. https://doi.org/10.1073/pnas.94.13.6579

[9] Shibata, H. and Ogata, N. (2016) *American Journal of Modern Physics*, **5**, 142-145. https://doi.org/10.11648/j.ajmp.20160505.14

[10] Hawking, S.W. (1974) *Nature*, **248**, 30-31. https://doi.org/10.1038/248030a0

[11] Krauss, L.M. and Scherrer, R.J. (2007) *General Relativity and Gravitation*, **39**, 1545-1550. https://doi.org/10.1007/s10714-007-0472-9

[12] Collins, C.B. and Hawking, S.W. (1973) *The Astrophysical Journal*, **180**, 317-334. https://doi.org/10.1086/151965

[13] Beltrán Almeida, J.P. and Pereira, J.G. (2006) *Physics Letters B*, **636**, 75-79. https://doi.org/10.1016/j.physletb.2006.02.069

[14] Daly, R.A. and Djorgovski, S.G. (2003) *The Astrophysical Journal*, **597**, 9-20. https://doi.org/10.1086/378230

[15] Barrow, J.D., Bean, R. and Magueijo, J. (2000) *Monthly Notices of the Royal Astronomical Society*, **316**, L41-L44. https://doi.org/10.1046/j.1365-8711.2000.03778.x

[16] Pandey, B. (2017) *Monthly Notices of the Royal Astronomical Society: Letters*, **471**, L77-L81. https://doi.org/10.1093/mnrasl/slx109

Scientific Research Publishing

Journal of Modern Physics, 2022, 13, 1267-1271
https://www.scirp.org/journal/jmp
ISSN Online: 2153-120X
ISSN Print: 2153-1196

Geometric Phase in General Relativity

Yossi Bachar[1*], Lawrence Horwitz[1,2,3]

[1]Department of Physics, Bar Ilan University, Ramat Gan, Israel
[2]School of Physics and Astronomy, Tel-Aviv University, Tel Aviv-Yafo, Israel
[3]Department of Physics, Ariel University at the Shomron, Shomron, Israel
Email: *yossi_dk@yahoo.com

How to cite this paper: Bachar, Y. and Horwitz, L. (2022) Geometric Phase in General Relativity. *Journal of Modern Physics*, **13**, 1267-1271.
https://doi.org/10.4236/jmp.2022.139075

Received: July 7, 2022
Accepted: September 4, 2022
Published: September 7, 2022

Abstract

We study the transport of a small wave packet in the embedding of the Stueckelberg-Horwitz-Piron relativistic quantum theory into the manifold of general relativity around the Schwarzschild solution using a semiclassical approximation. We find that the parallel transport of the momentum leads to a geometrical (Berry type) phase.

Keywords

Geometrical Phase, Quantum Theory in General Relativity, Schwarzschild Solution

In this paper, we study the idea called geometric (Berry) phase found by Berry in 1984 [1] in the context of electromagnetism, in application to the effect of a change in direction of the momentum vector parallel transported around a closed path on a manifold with curvature, such as in gravitational field [2] (see also [3] [4] [5]). This change, as we show, leads to a phase change on its wave function [6] in the quantum theory [7] (see also [8] and [9]).

Stone *et al.* [10] have discussed the geometrical and Berry phase associated with Dirac and Weyl particles; our work deals with the phase generated by parallel transport for a quantum theory on the manifold of general relativity. Ghosh and Mukhopadhyay [11] have discussed the geometric (Berry) phase for a Dirac Hamiltonian theory in a gravitational field, pointing out the similarities between the effects of gravitation and magnetism. We study here the geometrical (Berry) phase on a wave function associated directly with a rigorous quantum theory on the manifold. In this paper, we follow a narrow wave packet transported on a geodesic around a black hole [12] and show that a semicassical argument leads to such a geometrical phase.

For any conserved vector S_μ infinitesimal parallel transport along a geodesic is given by

$$\mathrm{d}S_\mu = -\Gamma^\lambda_{\mu\nu}\mathrm{d}x^\nu S_\lambda \tag{1}$$

where $\mathrm{d}x^\mu$ is along the curve. For the Schwarzchild coordinates t, r, θ, φ, we assume a geodesic circle [12] at constant t, θ and r and carry out the integration over φ with measure $\mathrm{d}\varphi$. The change in the vector with φ is

$$\mathrm{d}S_\mu = -\Gamma^\lambda_{\mu\varphi}\mathrm{d}\varphi S_\lambda \tag{2}$$

The only non-vanishing components that enter (*e.g.* [2]) are:

$$\begin{aligned}\Gamma^\varphi_{r\varphi} &= \frac{1}{r}\\ \Gamma^\varphi_{\theta\varphi} &= \cot\theta\\ \Gamma^\theta_{\varphi\varphi} &= -\sin\theta\cos\theta\end{aligned} \tag{3}$$

The parallel transport equations can then be written

$$\begin{aligned}\frac{\mathrm{d}S_r}{\mathrm{d}\varphi} &= -\frac{1}{r}S_\varphi\\ \frac{\mathrm{d}S_\theta}{\mathrm{d}\varphi} &= -\cot\theta S_\varphi\\ \frac{\mathrm{d}S_\varphi}{\mathrm{d}\varphi} &= \sin\theta\cos\theta S_\theta\end{aligned} \tag{4}$$

Due to the non-diagonal structure, we see that this system is, in fact, second order. At fixed θ, r, differentiating the second and third equations of (4), with respect to φ, we obtain

$$\begin{aligned}\frac{\mathrm{d}^2S_\theta}{\mathrm{d}\varphi^2} &= -k^2S_\theta\\ \frac{\mathrm{d}^2S_\varphi}{\mathrm{d}\varphi^2} &= -k^2S_\varphi\end{aligned} \tag{5}$$

where $k = |\cos\theta|$. The solutions of these oscillator type equations are given by

$$\begin{aligned}S_\theta &= A(\theta,r)\cos(k\varphi) + B(\theta,r)\sin(k\varphi)\\ S_\varphi &= C(\theta,r)\cos(k\varphi) + D(\theta,r)\sin(k\varphi)\end{aligned} \tag{6}$$

These solutions determine the equation for S_r:

$$\frac{\mathrm{d}S_r}{\mathrm{d}\varphi} = -\frac{1}{r}\left[C(\theta,r)\cos(k\varphi) + D(\theta,r)\sin(k\varphi)\right] \tag{7}$$

so that (up to a arbitrary function of θ, r, t which we set to zero).

$$S_r = -\frac{1}{kr}\left[C(\theta,r)\sin(k\varphi) - D(\theta,r)\cos(k\varphi)\right] \tag{8}$$

We must now set initial conditions at $\varphi = 0$. From Equation (6) we have

$$\begin{aligned}A(\theta,r) &= (S_\theta)_0\\ C(\theta,r) &= (S_\varphi)_0\end{aligned} \tag{9}$$

and from (8),

$$D(\theta,r)=kr(S_r)_0 \tag{10}$$

Since our equations are second order there must be just two independent constants of integration. One can eliminate, say, B, D, with initial conditions.

Using our solutions (6) and (8) and the original Equations (4), we see that

$$\begin{aligned}\left.\frac{\mathrm{d}S_r}{\mathrm{d}\varphi}\right|_0 &= -\frac{1}{r}C\\ \left.\frac{\mathrm{d}S_\theta}{\mathrm{d}\varphi}\right|_0 &= -\cot\theta = Bk\\ \left.\frac{\mathrm{d}S_\varphi}{\mathrm{d}\varphi}\right|_0 &= \sin\theta\cos\theta A = Dk\end{aligned} \tag{11}$$

so that, substituting for B and D, we have the solutions

$$\begin{aligned}S_\theta &= A\cos(k\varphi)-C\frac{\cot\theta}{k}\sin(k\varphi)\\ S_\varphi &= C\cos(k\varphi)+A\frac{\sin\theta\cos\theta}{k}\sin(k\varphi)\\ S_r &= -\frac{1}{kr}\left(C\sin(k\varphi)-A\frac{\sin\theta\cos\theta}{k}\cos(k\varphi)\right)\end{aligned} \tag{12}$$

with A and C given by the initial conditions (9) one finds the vector for any φ; and in particular for $\varphi=2\pi$ at any given θ for $k=|\cos\theta|$. Note that there is no singularity at $\theta=\pi/2$ ($k=0$). Substituting (9) into (12), and replacing S_μ by p_μ we obtain:

$$\begin{aligned}\Delta p_\varphi &= p_\varphi(\varphi=2\pi)-p_\varphi(\varphi=0)=\cos(2\pi k)-1+A(\theta,r)\frac{\sin\theta\cos\theta}{k}\sin(2\pi k)\\ \Delta p_\theta &= p_\theta(\varphi=2\pi)-p_\theta(\varphi=0)=A(\theta,r)(\cos(2\pi k)-1)-\frac{\cot\theta}{k}\sin(2\pi k)\\ \Delta p_r &= p_r(\varphi=2\pi)-p_r(\varphi=0)\\ &= -\frac{1}{kr}\left[\sin(2\pi k)+A(\theta,r)\sin\theta\cos\theta\cos(2\pi k)\left(1+\frac{1}{k}\right)\right]\end{aligned} \tag{13}$$

Therefore, after transport in φ from 0 to 2π,

$$\begin{aligned}p'_\varphi &= p_\varphi(\varphi=2\pi)=p_\varphi(\varphi=0)+\Delta p_\varphi = p_\varphi+\Delta p_\varphi\\ p'_\theta &= p_\theta(\varphi=2\pi)=p_\theta(\varphi=0)+\Delta p_\theta = p_\theta+\Delta p_\theta\\ p'_r &= p_r(\varphi=2\pi)=p_r(\varphi=0)+\Delta p_r = p_r+\Delta p_r\end{aligned} \tag{14}$$

This means that the momentum after parallel transport is equal to the original momentum plus the change Δp_μ found explicitly in Equation (13). Now, for a wavepacket narrow in both energy-momentum and spacetime, we assume that the classical computations are a good semiclassical approximation. For a wave packet of the form [6]:

$$\psi(x^\mu)=\frac{1}{\sqrt{4\pi\hbar}}\int \mathrm{d}^4 p_\mu \Phi(p_\mu)\mathrm{e}^{ip_\mu x^\mu/\hbar} \tag{15}$$

We have then

$$\Phi\left(p_\mu\right)=\frac{1}{\sqrt{4\pi\hbar}}\int \mathrm{d}^4 x_\mu \psi\left(x_\mu\right)\mathrm{e}^{-\mathrm{i}p_\mu x^\mu/\hbar} \tag{16}$$

where $x^\mu=\left(t,r,\theta,\varphi\right)$

After the change in the momentum in transport of the function from 0 to 2π in φ, we obtain

$$\begin{aligned}\Phi\left(p'_\mu\right)&=\frac{1}{\sqrt{4\pi\hbar}}\int \mathrm{d}^4 x_\mu \psi\left(x_\mu\right)\mathrm{e}^{-\mathrm{i}p'_\mu x^\mu/\hbar}\\&=\frac{1}{\sqrt{4\pi\hbar}}\int \mathrm{d}^4 x_\mu \psi\left(x_\mu\right)\mathrm{e}^{-\mathrm{i}\left(p_\mu+\Delta p_\mu\right)x^\mu/\hbar}\\&=\frac{1}{\sqrt{4\pi\hbar}}\int \mathrm{d}^4 x_\mu \psi\left(x_\mu\right)\mathrm{e}^{-\mathrm{i}p_\mu x^\mu/\hbar}\mathrm{e}^{-\mathrm{i}\Delta p_\mu x^\mu/\hbar}\\&=\Phi\left(p_\mu\right)\mathrm{e}^{-\mathrm{i}\Delta p_\mu x^\mu/\hbar}\end{aligned} \tag{17}$$

where $p_\mu=\left(E,p_r,p_\theta,p_\varphi\right)$.

We remark that a convolution is not necessary since the support of the wave packet is very narrow.

Now substitute this result into the expression for $\psi\left(x^\mu\right)$ in (15) at the initial point x^μ at $\varphi=2\pi$ to obtain the additional phase factor $\mathrm{e}^{-\mathrm{i}\Delta p_\mu x^\mu/\hbar}$.

$$\psi'\left(x^\mu\right)=\psi\left(x^\mu\right)\mathrm{e}^{-\mathrm{i}\Delta p_\mu x^\mu/\hbar}$$

We therefore find, in our semiclassical calculation, that a wave packet transported on a closed geodesic curve around a black hole acquires a geometrical (Berry type) phase. Quantum scattering [6] on a black hole should display, as for the Aharonov-Bohm [13] experiment, a corresponding interference effect.

Conflicts of Interest

The authors declare no conflicts of interest regarding the publication of this paper.

References

[1] Berry, M.V. (1984) *Proceedings of the Royal Society A*, **392**, 45-57. https://doi.org/10.1098/rspa.1984.0023

[2] Weinberg, S. (1972) Gravitation and Cosmology, Principles and Applications of the General Theory of Relativity. John Wiley & Sons, Inc., Hoboken, p. 336.

[3] Thompson, R. and Rapini, G. (1993) Berry's Phase and Gravitational Waves. *Proceeding of the* 5*th Canadian Conference on General Relativity and Relativistic Astrophysics*, Singapore, 13-15 May 1883.

[4] Sakurai, J.J. (2005) Modern Quantum Mechanics. Addison-Wesley, New York.

[5] Resta, R. (2000) *Journal of Physics: Condensed Matter*, **12**, R107. https://doi.org/10.1088/0953-8984/12/9/201

[6] Horwitz, L.P. (2019) *The European Physical Journal Plus*, **134**, 313. https://doi.org/10.1140/epjp/i2019-12689-7

[7] Chang, M.-C. and Niu, Q. (2008) *Journal of Physics: Condensed Matter*, **20**, Article

ID: 193202. https://doi.org/10.1088/0953-8984/20/19/193202

[8] Venturi, G. (1990) Quantum Gravity and the Berry Phase. In: *Differential Geometric Methods in Theoretical Physics*, Springer, New York, 703-713. https://doi.org/10.1007/978-1-4684-9148-7_69

[9] Mukhopadhyay, B. and Kanti Ganguly, S. (2020) *Universe*, **160**, Article ID: 6100160. https://doi.org/10.3390/universe6100160

[10] Stone, M., Dwivedi, V. and Zlou, T. (2015) *Physical Review D*, **91**, Article ID: 025004. https://doi.org/10.1103/PhysRevD.91.025004

[11] Ghosh, T. and Mukhopadhyay, B. (2020) *International Journal of Modern Physics D*, **30**, Article ID: 2150090. https://doi.org/10.1142/S0218271821500905

[12] Ludwin, D.M. and Horwitz, L.P. (2011) *Journal of Mathematical Physics*, **52**, Article ID: 012303. https://doi.org/10.1063/1.3533399

[13] Aharonov, Y. and Bohm, D. (1959) *Physical Review*, **115**, 485. https://doi.org/10.1103/PhysRev.115.485

Journal of Modern Physics, 2022, 13, 1272-1286
https://www.scirp.org/journal/jmp
ISSN Online: 2153-120X
ISSN Print: 2153-1196

Study of Dissipating of Wave Energy in the Breakers Zone of the Gulf of Guinea: Case of Autonomous Port of Cotonou in Benin Coastal Zone

Oswald G. Acclassato[1,2], Noukpo Bernard Tokpohozin[1,3,4*], Christian D. Akowanou[3], Adjimon Mathias Houékpohéha[1,4], Guy Hervé Houngue[1,2], Bruno Basile Kounouhéwa[1,3,4]

[1]Laboratoire de Physique du Rayonnement FAST-UAC, Cotonou, République du Bénin
[2]Département de Physique (FAST) et Formation Doctorale Sciences des Matériaux (FDSM/UAC), Calavi, République du Bénin
[3]Institut National Supérieur des Classes Préparatoires aux Etudes d'Ingénieur (INSPEI/UNSTIM), Abomey, République du Bénin
[4]Institut de Mathématiques et de Sciences Physiques (IMSP/UAC), Porto-Novo, République du Bénin
Email: *donaelfreed@gmail.com, acclassat@yahoo.fr, christianakowanou@gmail.com, mathias.houekpoheha@imsp-uac.org, hguyherv@gmail.com, kbbasile@gmail.com

How to cite this paper: Acclassato, O.G., Tokpohozin, N.B., Akowanou, C.D., Houékpohéha, A.M., Houngue, G.H. and Kounouhéwa, B.B. (2022) Study of Dissipating of Wave Energy in the Breakers Zone of the Gulf of Guinea: Case of Autonomous Port of Cotonou in Benin Coastal Zone. *Journal of Modern Physics*, **13**, 1272-1286.
https://doi.org/10.4236/jmp.2022.139076

Received: May 22, 2022
Accepted: September 13, 2022
Published: September 16, 2022

Abstract

Rapid population growth and major trends of world economy growth have led to significant energy needs in our country. Benin, Gulf of Guinea country, although with a significant coastal network powered by potential energy from breaking waves, has experienced a deficit and a critical energy instability, marked by recurrent power cuts and disruption of the national economy. To ensure the integration of this source of renewable energy in the Benin energy mix and sustainably reduce the energy deficit in progress, this work has aimed to study the dissipation of wave energy at the bathymetric breaking in the breakers zone of Cotonou coast. Sea conditions and the statistics parameters of the breaking waves under perturbation effect of the seabed were evaluated to predict the beginning of the breaking. The modeling is based on the Navier-Stokes equation in which the viscosity and the interactions between the molecules of the oceanic fluid are neglected. The nonlinear wave dispersion relation is also used. The results obtained for this purpose showed that water particles have an almost parabolic motion during their fall; their velocity is higher than those of the early breaking. In this area, the waves dissipate about 80% of their energy: it generates turbulence which leads to a strong setting in motion of sediments.

Keywords

Wave, Breaker Zone, Wave Power, Energy Dissipation, Seabed

1. Introduction

Waves are oscillations of the sea surface, generated by the wind energy and maintained by gravity [1]. The profile of a wave can change under the effect of an external disturbance (wind, seabed…). It may encounter some movements, such as shoaling, breaking, refraction, diffraction, reflection… [2]. Waves carry a significant amount of energy which derives from the force of wind upon the seas around the globe and that is dispersed by the bathymetric breaking on coasts: they are renewable energy sources. Waves' breaking is a key aspect of the dynamics of sea states, particularly in the coastal dynamics. The dissipative processes, including the breaking, constitute one of the important terms of the energy balance sheet to the wave field and require appropriate definition in calculating the sea conditions. However, breaking is still poorly understood and poorly defined.

Benin is a coastal state of the Gulf of Guinea. As such, it has access to the ocean which is at the core of perpetual wave motions [3]. Despite the important population growth, Benin has been experiencing, for nearly two decades, a significant and recurring energy crisis characterized by long periods of power cut owing to a significant energy deficit. To this end, it turns out to be essential to explore its energy sources. Marine dynamic is a source yet not well-researched and undeveloped in Benin. Oceans are rich in energy flows that can be exploited [4]. Characterization of the breakers zone has been done on Benin coast based on data of MCA Benin, Navier-Stokes equation, and dispersion relation of non-linear waves. An analysis of the energy dispersion rate of wave energy carried out in this area shows that it represents the dissipation zone par excellence for breaking waves. The study of variation of the group velocity in the area reveals that water particles enrolled at the breaking accelerate and drop with a velocity higher than that of the early breaking. Finally, the horizontal length of the breakers zone and the fall period of enrolled particles are measured on the study site and a study has been carried out on their variation.

2. Material and Methods

2.1. Study Site and Data Used

The bathymetric map (**Figure 1(A)** below) obtained at the CBRST (Benin Centre for Scientific and Technical Research) shows the evolution of the local water depth in the coastal area of Benin and predicts the average slope and macroscopic variability of the seabed. This map shows that the seabed in the coastal area is almost flat and sloping. It is a gently sloping seabed $p = \tan\beta$ as $0.001 < \tan\beta \le 0.1 \Rightarrow \tan\beta \approx \beta$. The slope in the shoaling zone corresponds to the following on average $\beta_m \approx \frac{100}{2000} = 0.05$ [5].

Benin is a country of the Gulf of Guinea located between the parallel 6˚15' and 12˚30' north latitude the one hand and meridians 1˚ and 3˚40' east longitude on the other hand (**Figure 1(B-a)**) [6]. It has gotten a coastal area that is 125 km from Hillacondji in the west, to Krake in the east. Benin coast is more or less linear

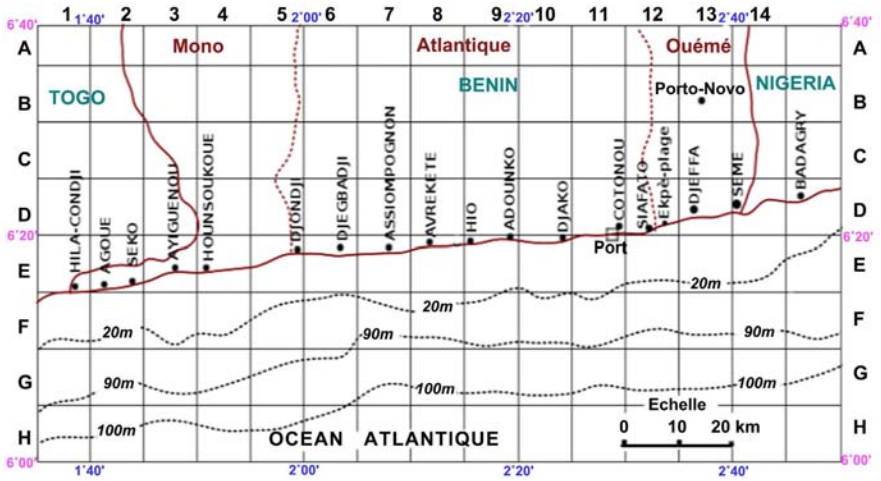

(A)

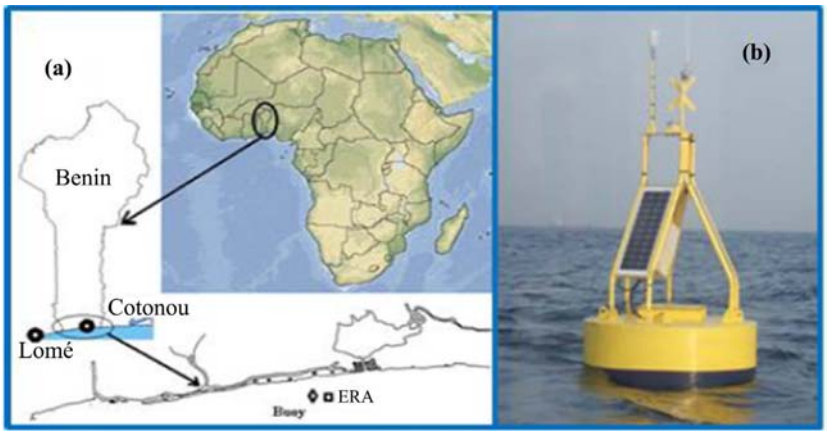

(B)

Figure 1. (A) Bathymetric map of Benin; (B) Sketch of study area (Benin, Gulf of Guinea). (a) Location of ERA and (b) oceanographic buoy.

and cut off in two places, namely, the Bouche du Roy and the channel mouth of Cotonou. Its coastal zone is between latitude 6˚15' and 6˚23' north [7].

Waves parameters, significant wave height (H_s) and peak period (T_p) are recorded every 30 min. The buoy data (**Figure 1(B-b)**) are used for ERA data validation and cover the period from December 2015 to October 2016 (See HOUNGUE *et al.*, 2018, for more descriptions).

The gravity on the coast of Benin is approximately $g = 9.80\ \mathrm{N/kg}$ and the density of sea water is $\rho = 1025\ \mathrm{kg/m^3}$ [8].

As part of the expansion of the port of Cotonou, the Millennium Challenge Account-Benin (MCA-Benin) performed a series of measures in terms of wave power. These measures are performed with two stations of wave recorder buoy called WCP1 and WCP2 whose geographical coordinates are respectively (N 6˚20.118'; E 2˚27.255') and (N 6˚20.373'; E 2˚26.140') [9].

Data analysis yielded the following diagrams which respectively reflect the period T (**Figure 2(A)**), the peak to valley height H (**Figure 2(B)**) and direction (**Figure 3**) of propagation of swells off the Benin coast [10].

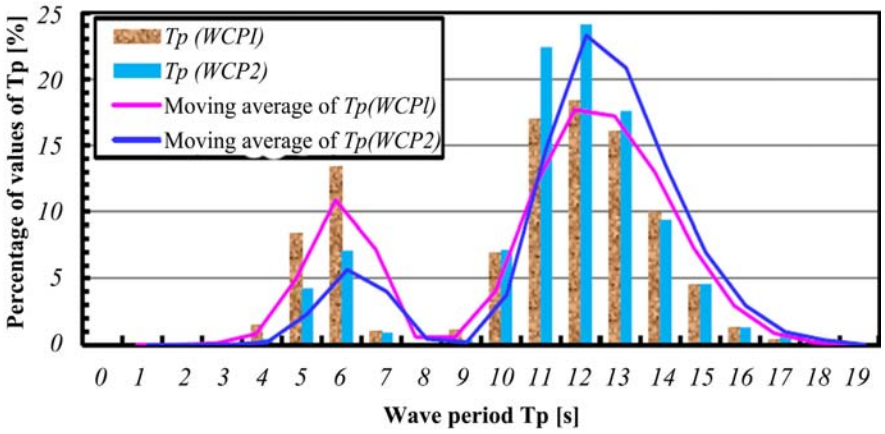

(A)

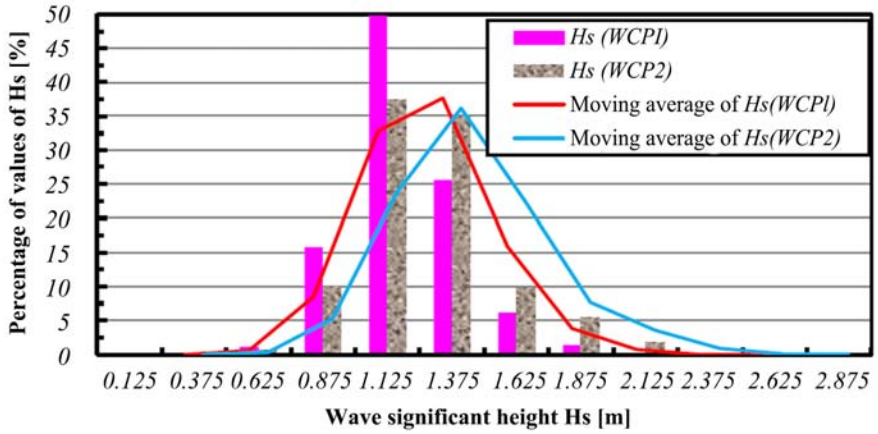

(B)

Figure 2. (A) Period of swells in the coastal zone of Benin; (B) Height of swells in the coastal zone of Benin.

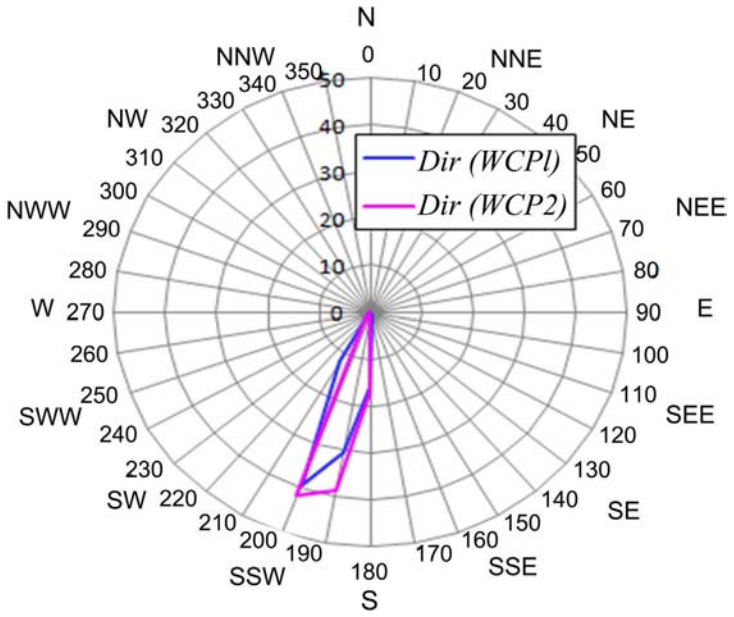

Figure 3. Propagation direction of swells in Benin coastal zone.

From the analysis of these curves, it appears that the swells in the Gulf of Guinea in Cotonou have:

- ✓ A height which varies between 0.4 m and 2 m (0.4 m ≤ H_o ≤ 2 m) with a common average value of about 1.1 m ($H_{om} \approx 1.1$ m);
- ✓ A period of peak that ranges between 8 s and 18 s (8 s ≤ $T \leq 18$ s) and whose average value is about 12 s ($T_m \approx 12$ s);
- ✓ A propagation direction that lies between the south (S) and southwest (SW) with a strong dominance of the direction from the south to the southwest (SSW).

As for the sea breeze or short swells generated by local winds, they have a period that varies between 3 s and 7 s.

2.2. Swell Velocity at Breaking Point

When swells become nonlinear under the effect of shoaling (lifting of swell), refraction, reflection, diffraction... it is induced by the disturbing effect of the seabed, the wave dispersion relation proposed by Dalrymple *et al.*, to improve angularity [11] [12].

$$\omega^2 = gk\tanh(kh) \tag{1}$$

with $h = d + \frac{H}{2}$

Group velocity $C_g = \frac{\partial\omega}{\partial k}$ and phase velocity $C_\varphi = \frac{\omega}{k}$ have been inferred from that relation of nonlinear dispersion [13].

Bathymetric breaking occurs in shallow waters where $\tanh(kh) \approx kh$; thus we have.

$$C_g = C_\varphi = \sqrt{g\left(d + \frac{H}{2}\right)} \tag{2}$$

Using the results obtained with the theory of Boussinesq and the breaking standard of Kaminsky and Krauss (1993) [14], the local depth of water d_b, the height of wave H_b and the wavelength L_b at the breaking point [15] and where H_o and $L_o = \frac{gT^2}{2\pi}$ represent the off height and wavelength.

$$\begin{cases} d_b = \dfrac{H_o^{0.908} L_o^{0.092}}{1.33(\tan\beta)^{0.216}} \\ H_b = 0.903 H_o \left(\dfrac{L_o}{H_o}\right)^{0.227} (\tan\beta)^{0.054} \\ L_b = \dfrac{0.613 T^2 H_o^{0.454} L_o^{-0.459}}{\pi(\tan\beta)^{0.108}} \end{cases}$$

$$\Rightarrow \mu_b = \frac{d_b}{L_o} = \frac{H_o^{0.908} L_o^{-0.918}}{1,33(\tan\beta)^{0.216}} \tag{3}$$

Thus at the breaking point, we have:

$$C_{g_b} = C_{\varphi_b} = \sqrt{g\left(d_b + \frac{H_b}{2}\right)} \tag{4}$$

2.3. Modeling of Breaking in the Breakers Zone

The breakers zone is the area where swells break for the first time. In this area, the vertical rise of the free surface behaves like a wave of expansion during the breaking. When the maximum height obtained begins to drop at the end of shoaling, water particles located on the surface follow the break and drop sharply.

2.3.1. Position, Velocity and Trajectory of the Water Particles Affected

The forces of pressure and gravity and that of Coriolis caused by viscosity make it possible to establish the Navier-Stokes equation below [10].

$$\frac{\partial \boldsymbol{u}}{\partial t} + (\boldsymbol{u}\cdot\nabla)\boldsymbol{u} = -\frac{1}{\rho}\nabla p + \boldsymbol{g} + \frac{\mu}{\rho}\Delta\boldsymbol{u} \tag{5}$$

So, the acceleration $\boldsymbol{a}$ of dropping particles is:

$$\boldsymbol{a} = \frac{\mathrm{d}\boldsymbol{u}}{\mathrm{d}t} = \frac{\partial \boldsymbol{u}}{\partial t} + (\boldsymbol{u}\cdot\nabla)\boldsymbol{u} = \frac{1}{\rho}\nabla p + \boldsymbol{g} - \frac{\mu}{\rho}\Delta\boldsymbol{u} \tag{6}$$

At the surface, the pressure is nearly constant and equal to the atmospheric pressure ($p = p_{atm} = Cste \Rightarrow \nabla p \to \mathbf{0}$). As the viscosity μ is negligible compared to the density ρ of the ocean ($\mu \ll \rho \Rightarrow \frac{\mu}{\rho} \to 0$), we obtain the following [15]:

$$\boldsymbol{a} = \boldsymbol{g} \tag{7}$$

By approximating the direction of swell spread to a straight line, the wave's position $\boldsymbol{r}$ and its velocity $\boldsymbol{v}$ are specified on the mark $(O, \boldsymbol{i}, \boldsymbol{k})$ such as the origin O (Figure 4), taken at the free surface of a calm ocean, coincides with the start of the breakers zone (as shown in the figure below).

At the breaking point, the height of the wave is H_b and its group velocity C_{g_b}. Therefore, the early breaking begins at a position $\boldsymbol{r}_o$ with a velocity $\boldsymbol{u}_1$ as.

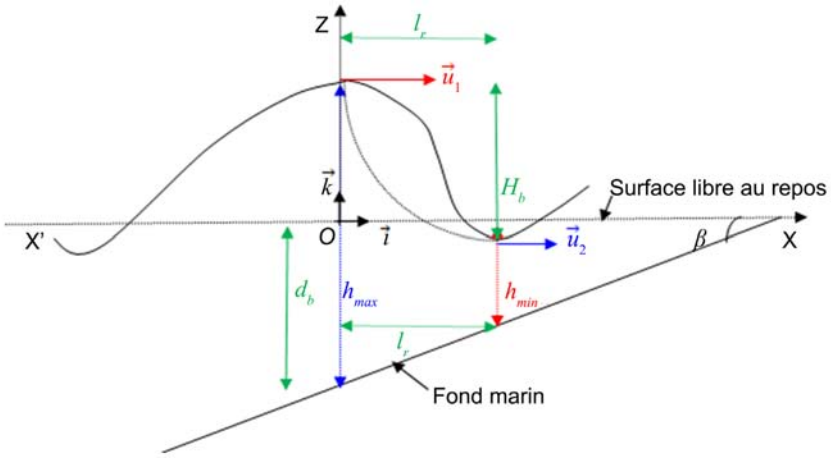

Figure 4. Wave in the breakers zone.

$$\boldsymbol{r}_o \begin{cases} x_o = 0 \\ z_o > 0 \end{cases} \text{ and } \boldsymbol{u}_1 \begin{cases} u_{1x} = C_{g_b} \\ u_{1z} = 0 \end{cases} \tag{8}$$

The position and velocity are respectively given by:

$$\boldsymbol{r}(x,z) = -\frac{1}{2}\boldsymbol{a}t^2 + \boldsymbol{u}_1 t + \boldsymbol{r}_o$$

$$\Rightarrow \boldsymbol{r}(x,z) \begin{cases} x(t) = C_{g_b} t \\ z(t) = \eta(t) = -\frac{1}{2} g t^2 + z_o \end{cases} \tag{9}$$

$$\boldsymbol{u} = \frac{\mathrm{d}\boldsymbol{r}}{\mathrm{d}t} \Rightarrow \boldsymbol{u}(x,z) \begin{cases} u_x = C_{g_b} \\ u_z = -gt \end{cases} \tag{10}$$

Thus, the path equation of the water particles located at the surface during the breaking in the breakers zone is:

$$\eta(x) = z = -\frac{1}{2d_b + H_b} x^2 + \frac{H_b}{2} \text{ with } 0 \le x \le l_r \tag{11}$$

2.3.2. Fall time t_c, Length of Breakers Zone l_r, and Local Depth of Water d_c at the Sloping Point

If at the end of the breakers zone the particles renew contact with the ocean at a point $\boldsymbol{r}_C$ with a velocity $\boldsymbol{u}_c$ and a horizontal component $\boldsymbol{u}_2$, then we get the following:

$$\boldsymbol{r}_C \begin{cases} x_C = l_r \\ z_C \le 0 \end{cases} \text{ and } \boldsymbol{u}_c \begin{cases} u_{Cx} = u_2 = C_{g_b} \\ u_{Cz} = -gt_C \end{cases} \text{ with } H_b = z_C - z_o \tag{12}$$

At the end of a time t_C, the particle slopes on the free surface at rest and twist it towards the depth at a position $\boldsymbol{r}_c(l_r, z_c)$; thus we obtain:

$$\boldsymbol{r}_c(l_r, z_c) \begin{cases} l_r = C_{g_b} t_C \\ z_c = -\frac{1}{2} g t_C^2 + z_o \end{cases} \Rightarrow \begin{cases} l_r = \sqrt{H_b(2d_b + H_b)} \\ t_C = \sqrt{\frac{2H_b}{g}} \end{cases} \tag{13}$$

The local depth of water d_c at the sloping point is as:

$$d_c = d_b - l_r \tan\beta = d_b - \sqrt{H_b(2d_b + H_b)} \tan\beta \tag{14}$$

2.3.3. Variation in Group Velocity and Wave Energy in the Breakers Zone

From the previous results, we have:

$$C_g = u = \sqrt{C_{g_b}^2 + g^2 t^2} = C_{g_b} \sqrt{1 + \frac{g^2 t^2}{C_{g_b}^2}} \text{ if } 0 \le t \le t_C \tag{15}$$

Let $\delta_v = \frac{C_g}{C_{g_b}}$ be the coefficient of variations of the group velocity in the zone

$$\delta_v = \frac{C_g}{C_{g_b}} = \sqrt{1 + \frac{2gt^2}{2d_b + H_b}} \text{ with } 0 \le t \le \sqrt{\frac{2H_b}{g}} \tag{16}$$

If C_{gc} is the velocity of particles at the sloping point, then the ratio $\delta_{vc} = \dfrac{C_{gc}}{C_{g_b}}$ expressing the variations in velocity between the end and the beginning of the breakers zones is given by:

$$\delta_{vc} = \frac{C_{gc}}{C_{g_b}} = \sqrt{1 + \frac{2gt_c^2}{2d_b + H_b}} \quad \text{with } t_c = \sqrt{\frac{2H_b}{g}}$$

$$\Rightarrow \delta_{vc} = \frac{C_{gc}}{C_{g_b}} = \sqrt{1 + \frac{4}{1 + \dfrac{2d_b}{H_b}}} \tag{17}$$

2.3.4. Energy Dissipation Rate in the Breakers Zone

The total energy carried by a swell is given by:

$$E = \frac{1}{8}\rho g H^2 \tag{18}$$

when the breaking ends (in Surf and Swash zones) where $d \le d_b$, the height of wave drops if the local depth of water d falls; according to Bonneton P. 2002, this is expressed by the relation below:

$$H(d) = H_b \left[\sigma \left(\frac{d}{d_b} \right)^{-\frac{1}{2}} + (1-\sigma) \left(\frac{d}{d_b} \right)^{\frac{1}{4}} \right]^{-1} \tag{19}$$

with $\sigma = \dfrac{2H_b}{T \tan\beta \sqrt{g\left(d_b + \dfrac{H_b}{2}\right)}}$

H_b and d_b are respectively the height of swell and the local depth of water at the bathymetric breaking point. Thus, we obtain the following at the first dropping point of enrolled water particles:

$$H_c = H_b \left[\sigma \left(\frac{d_c}{d_b} \right)^{-\frac{1}{2}} + (1-\sigma) \left(\frac{d_c}{d_b} \right)^{\frac{1}{4}} \right]^{-1} \tag{20}$$

with $\sigma = \dfrac{2H_b\sqrt{2}}{T \tan\beta \sqrt{g\left(2d_b + H_b\right)}}$

Let $\tau_d = \dfrac{E_{wb} - E_{wc}}{E_{wb}}$ be the dissipated energy rate in the breakers zone during the breaking where E_{wb} and E_{wc} represent respectively the total energy at the beginning and at the end of the breakers zone.

$$\Rightarrow \tau_d = 1 - \left(\frac{H_c}{H_b} \right)^2$$

$$\Rightarrow \tau_d = 1 - \left[\sigma \left(1 - \frac{l_r \tan\beta}{d_b} \right)^{-1/2} + (1-\sigma) \left(1 - \frac{l_r \tan\beta}{d_b} \right)^{1/4} \right]^{-2} \tag{21}$$

3. Results and Discussion

3.1. Presentation of the Results

Graphs of Figure 5 show the variations in horizontal length l_r of the breakers zone and the fall time t_c of water particles according to the off height and wave period in the breakers zone at Cotonou. In terms of the graph in Figure 6, it reveals the influence of the slope of the seabed on the latter.

The curves in Figure 7 and Figure 8 below represent the variations in ratio δ_{vc} according to the height and period of waves on the one hand and the slope of the seabed on the other hand.

The graph below (Figure 9) expresses variations in ratio of the wave energy dissipation in the breakers zone for $\beta \approx 0.05$ rad . As for the graph in Figure 10, it highlights the influence of the slope of seabed on the dissipation on the energy.

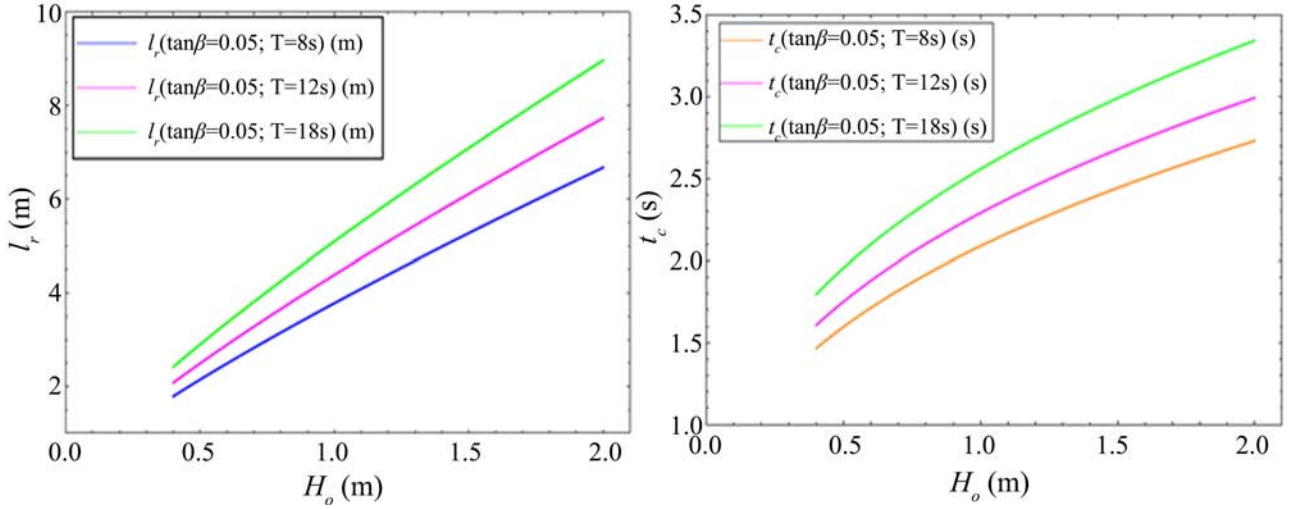

Figure 5. Variations in horizontal length l_r of breakers zone and water particles fall time t_c .

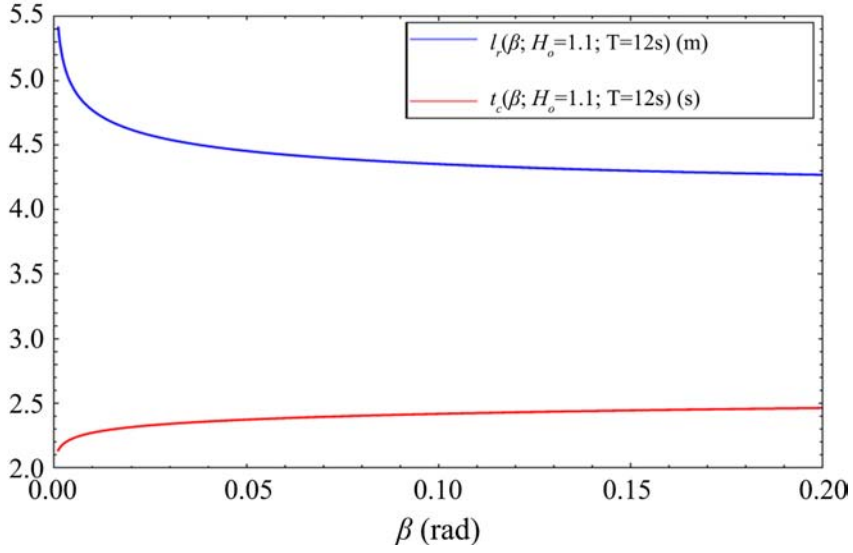

Figure 6. Influence of the seabed slope on the length l_r the time t_c .

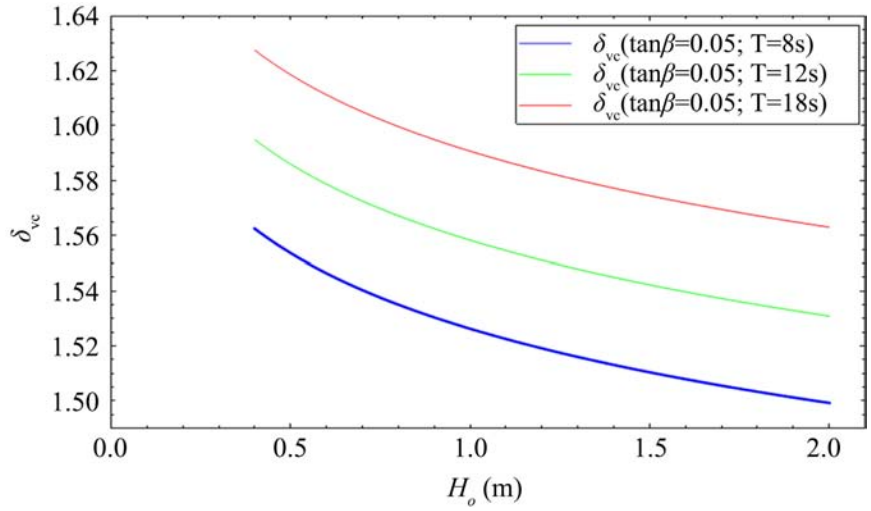

Figure 7. Coefficient δ_{vc} of variations in velocity of enrolled particles.

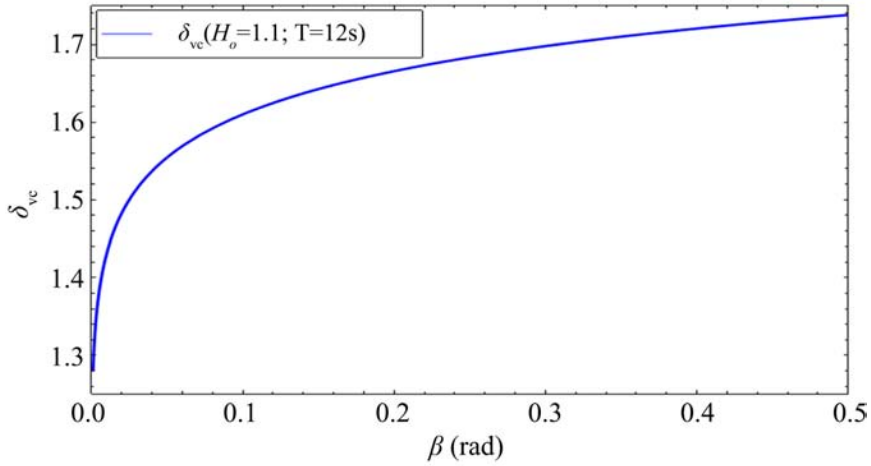

Figure 8. Influence of the slope of the seabed on δ_{vc}.

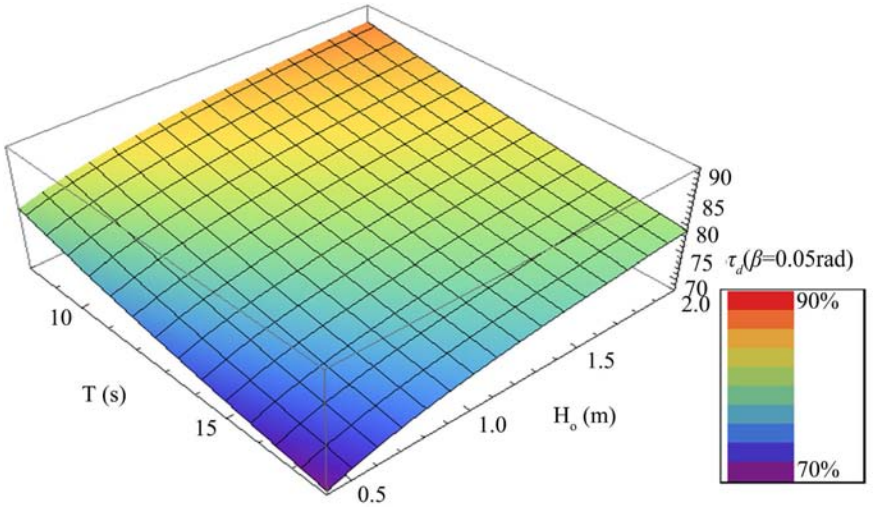

Figure 9. Variation in energy dissipation rate according to the off height and wave period.

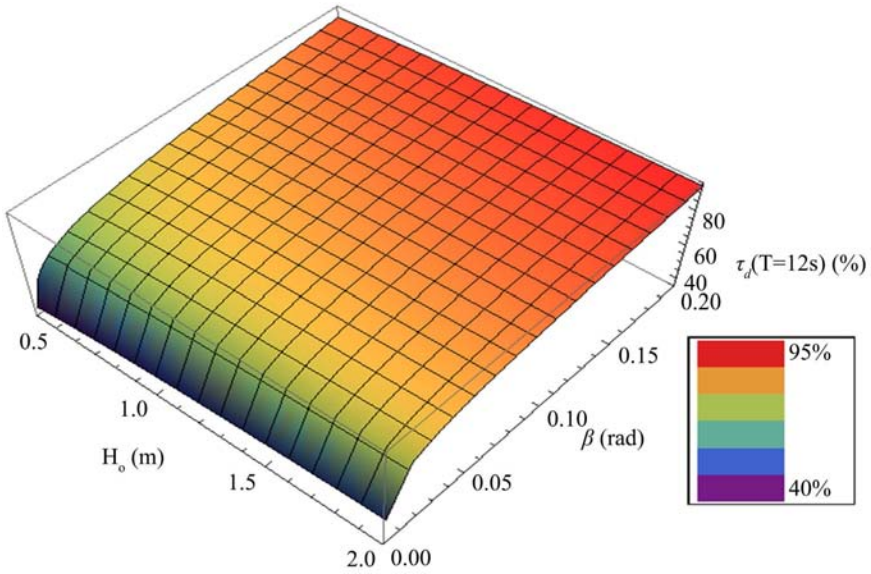

Figure 10. Influence of the slope of the seabed on energy dissipation in breakers zone.

3.2. Analysis and Discussion of Findings

The curves of **Figure 5** which present the variations of length horizontally from the breakers zone and the sloping duration of enlisted water particles, show that these two quantities increase according to the off height and wave period when the average slope of the seabed is $\tan\beta \approx 0.05$. On the site, when the period fluctuates between 8 s and 18 s and then the height is between 0.4 m and 2 m:

- The horizontal length l_r of the breakers zone varies between 2 m and 7 m approximately ($2\text{ m} \le l_r \le 7\text{ m}$).
- The fall duration of the water particles fluctuates between 1.5 s and 3.5 *s* approximately ($2\text{ s} \le t_c \le 2.5\text{ s}$).
- Variations of the curves in **Figure 6** show that l_r drops when the slope of the seabed rises whereas t_c falls. When the slope β of the seabed to the horizontal varies between 0.001 rad and 0.2 rad with $H_o = 1.1\text{ m}$ and $T = 12\text{ s}$:

- The length l_r varies between 5.5 m and 4.3 m approximately ($4.3\text{ m} \le l_r \le 5.5\text{ m}$).
- The fall time t_c corresponds to figures between 2 s and 2.5 s approximately ($2\text{ s} \le t_c \le 2.5\text{ s}$).

Variations in the coefficient δ_{vc} (**Figure 7**) which reflects the ratio of water particles velocity at the end and beginning of the breakers zone reveal that:

- $\delta_{vc} > 1 \quad \forall T, H_o$ and β: therefore the velocity acquired by the water particles at the end of the breakers zone is always higher than their velocity at the beginning of this zone; the velocity of the particles increases in the breakers zone.
- δ_{vc} is a monotonic function of the wave period T but a descending function of their off height H_o: the longer the period is (the smaller the height of swell is), the more important the velocity of water particles is in the breakers zone.

The evolution of the curve of Figure 8 related to the influence of the slope of the seabed on δ_{vc} states that this coefficient is a monotonic function of the slope of the seabed. But this growth tends a limit when $\tan\beta \to 1 \Rightarrow 0 \le \beta \le \frac{\pi}{4}$.

The graph of Figure 9 shows the variations in dissipation rate τ_d of the swell energy according to their off height and period in the breakers zone on the coast of Benin. Its evolution reveals that:

- The dissipation rate increases with the off height of the swells; it is therefore a monotonic function of the wave height.
- The rate decreases as the frequency of these waves increases: it is a decreasing function of the period.
- Each breaking wave loses between 70% and 90% of their energy in the breakers zone in Cotonou with an average slope $\tan\beta \approx 0.05$ when the period fluctuates between 8 s and 18 s and the height between 0.4 m and 2 m.
- Breaking is the major source of dissipation of wave energy on the study site.

As for the diagram of Figure 10 which shows the influence of the slope of the seabed on the dissipation rate τ_d of the wave energy, one can read that:

- The dissipation of the breaking waves energy in the breakers zone increases with the slope of the seabed.
- On the study site, when $T = 12\text{ s}$ and $0.4\text{ m} \le H_o \le 2\text{ m}$, the rate of dissipation varies between 40% and 95% as the slope of the seabed to the horizontal varies between 0.001 rad and 0.2 rad.

4. Conclusions

Dissipation of breaking wave energy is a shaft of renewable energy. It appears from this study that the breaking waves in the breakers zone at the coast of Benin lose about 80% of their total energy. This generates turbulence on this site, and leads to a strong set in motion of non-cohesive sediments: it heightens coastal erosion that one can observe on this coast. This dissipation increases with the off height of waves but decreases with their period; it is a monotonic function of the slope of the seabed. In addition, results show that the horizontal length l_r of the breakers zone is an increasing function of the period and the wave height can vary between 2 m and 7 m. As for the fall time of the water particles in this zone, it fluctuates between 1.5 s and 3.5 s. Similarly, the velocity of the water particles increases in this zone depending on the period of the swells and the slope of the seabed but constitutes a decreasing function of their off height H_o.

In Benin context characterized by a large energy deficit, the development of this sea renewable energy would be a good perspective to address the crisis and improve the modern conveniences of the country in terms of energy.

Acknowledgements

The authors thank Benin Center for Scientific Research and Innovation (CBRSI) for accompanying this research work.

Conflicts of Interest

Authors have declared that no competing interests exist.

We (Author and Co-Authors) confirm that neither the manuscript nor any part of its contents is currently under review or published in any other journal. All authors (Author and Co-Authors) have approved the manuscript and are in agreement with its submission to JMP.

References

[1] Bonneton, P. (2001) *Comptes Rendus de l'Académie des Sciences - Series IIB - Mechanics*, **329**, 27-33. https://doi.org/10.1016/S1620-7742(00)01278-2

[2] Ardakani, A. and Bridges, J. (2010) Shallow Water Sloshing in Rotating Vessels Undergoing Prescribed Rigid-Body Motion in Two Dimensions. Department of Mathematics, University of Surrey, Guildford, 1-48.

[3] Kounouhewa, B.B., Tokpohozin, N.B., Houekpoheha, A.M., Awanou, C.N. and Chabi-Orou, B.J. (2014) *Journal de la Recherche Scientifique de l'Université de Lomé*, *Serie E*, **16**, 527-536.

[4] Bonneton, P. (2003) *Revue Française de Génie Civil*, **7**, 1061-1076. https://doi.org/10.1080/12795119.2003.9692534

[5] Houekpoheha, A.M., Kounouhewa, B.B., Hounsou, J.T., Tokpohozin, N.B. and Awanou, C.N. (2015) *Revue des Energies Renouvelables*, **18**, 89-103.

[6] Houekpoheha, A.M., Kounouhewa, B.B., Tokpohozin, N.B. and Awanou, C.N. (2014) *Revue des Energies Renouvelables*, **17**, 489-495.

[7] Abbasov, I.B. (2012) *Applied Mathematics*, **3**, 135-141. https://doi.org/10.4236/am.2012.32021

[8] Houékpohéha, M.A., Kounouhéwa, B.B., Hounsou, J.T., Tokpohozin, B.N., Hounguèvou, J.V. and Awanou, C.N. (2015) *International Journal of Renewable Energy Development*, **4**, 64-71. https://doi.org/10.14710/ijred.4.1.64-71

[9] Hervé Hounguè, G., Kounouhewa, B.B., Almar, R., Sohou, Z., Lefebvre, J.-P., Houépkonhéha, M. and Tokpohozin, B. (2018) *Journal of Coastal Research*, **81**, 130-137. https://doi.org/10.2112/SI81-017.1 http://www.JCRonline.org

[10] Kounouhewa, B.B., Houekpoheha, A.M., Tokpohozin, N.B., Awanou, C.N. and Chabi-Orou, B.J. (2014) Simulation of swell energy power in Autonomous Port of Cotonou. *Journal de la Recherche Scientifique de l'Université de Lomé*, *Serie E*, **16**, 183-193.

[11] Bougis J. (2004) Modèle d'approche de la houle par une méthode de refraction - Diffraction en coordonnées curvilignes. *Revue Paralia*, *VIIIème Journées Nationales Génie Civil-Génie Côtier*, Compiègne, 7-9 September 2004, 55-64. https://doi.org/10.5150/jngcgc.2004.007-B

[12] Babanin A.V. (2009) *Acta Physica Slovaca*, **59**, 305-535.

[13] Senechal, N. (2003) Etude de la propagation des vagues au-dessus d'une bathymétrie complexe en zone de surf. Thesis, No. 2759, Bordeaux I University, Bordeaux, 1-288.

[14] Sabatier, F. (2001) Fonctionnement et Dynamiques morpho-sédimentaires du littoral du Delta du Rhone. Doctoral Thesis, Thesis No. 0/1/A/I/X/3/0/1/0/3, AIX-Marseille II University (School of the Faculty of Science and Technology of Saint Jerome), Marseille.

[15] Tokpohozin, N.B., Kounouhéwa, B., Avossevou, G.Y.H., Houékpohéha, M.A. and Awanou, C.N. (2015) *Acta Oceanologica Sinica*, **34**, 137-142. https://doi.org/10.1007/s13131-015-0610-2

Abbreviations and Acronyms

ρ : Density of sea water (kg/m^3);
μ : Fluid dynamic viscosity (sea water);
$\boldsymbol{r}$: Vector position of a point located on the free surface;
η : Vertical elevation of the water level relative to the reference (m);
β : Inclination of the seabed relative to the horizontal (rad);
g: Gravity acceleration (m/s^2);
H: Wave crest-to-trough height (m);
H_0 : Offshore wave height peak to trough (m);
H_b : Wave crest-to-trough height at breaking point (m);
H_c : Peak-to-trough height of the swell in the breaker zone (m);
L: Wave length of the swell (m);
L_0 : Wavelength of the offshore swell (m);
L_b : Wavelength of the swell at the breaking point (m);
L_c : Wavelength of the swell in the breaker zone (m);
l_r : Horizontal length of the breaker zone (m);
$T = \frac{2\pi}{\omega}$: Swell period (s);
d: Surface-seabed distance near in coastal areas (m);
d_b : Local water depth at the breaking point (m);
d_c : Local water depth in the breaker zone (m);
C_g : Wave group speed (m/s);
C_φ : wave phase speed (m/s);
C_{gb} : Swell group speed at breaking point (m/s);
$C_{\varphi b}$: Swell phase speed at breaking point (m/s);
C_{gc} : Swell group speed in the breaker zone (m/s);
E: Total wave energy (J/m);
E_{wb} : Total energy at the start of the breakers zone (J/m);
E_{wc} : Total energy at the end of the breaker zone (J/m);
t_c : Duration of fall of water particles in the breakers zone (s);
$\tau_d = \frac{E_{wb} - E_{wc}}{E_{wb}}$: Rate of energy dissipated in the breakers zone;
$\delta_v = \frac{C_g}{C_{g_b}}$: Coefficient of variations of group speed in the breaker zone;
$\delta_{vc} = \frac{C_{gc}}{C_{g_b}}$: Rate of the speeds of the water particles enlisted at the end and at the start of the breakers zone.

Journal of Modern Physics, 2022, 13, 1287-1294
https://www.scirp.org/journal/jmp
ISSN Online: 2153-120X
ISSN Print: 2153-1196

Resolving Electron Mass Inconsistency Using Negative Mass

Arlen Young

Independent Researcher, Palo Alto, CA, USA
Email: arlen_young@yahoo.com

How to cite this paper: Young, A. (2022) Resolving Electron Mass Inconsistency Using Negative Mass. *Journal of Modern Physics*, **13**, 1287-1294.
https://doi.org/10.4236/jmp.2022.139077

Received: August 21, 2022
Accepted: September 16, 2022
Published: September 19, 2022

Abstract

In a previous publication, the author discussed the electron mass and charge inconsistencies resulting from classical models. A model was proposed using classical equations and two opposite charges to resolve the charge inconsistency. The model proposed in that article is modified herein using classical equations to define a model that also resolves the mass inconsistency. The positive mass of the outer shell of the electron core is replaced with a negative mass. The small negatively-charged core at the center still has positive mass.

Keywords

Classical Electron Model, Electron Radius, Electron Magnetic Dipole Moment, Electron Spin Angular Momentum, Negative Mass, Electron Mass Inconsistency, Electron Charge Inconsistency, Particle Physics

1. Introduction

Reference [1] addresses a great inconsistency between the measured electron spin magnet dipole moment and the moment calculated from spinning the electron charge. A similar inconsistency exits between the spin angular momentum derived from quantum theory [1] and the classical momentum calculated from spinning the electron mass [1]. The author proposed in [1] a classical model for resolving the magnetic dipole moment inconsistency. That same model is extended herein using classical physics equations to resolve the spin angular momentum inconsistency. The modified model has the following additional features:

- core having a negative mass outer shell and a positive mass inner core at the center;
- resolve the inconsistency between the spin angular momentum S and the momentum calculated from spinning the electron mass;

- no tensile or compressive forces on the core material for a ring shape;
- radius close to the classical radius;
- no intrinsic or induced electric dipole moment.

Except where otherwise noted, all constants and equations in this article are expressed in cgs units.

The shape of the electron in the model will first be assumed to be a ring. A spherical shape will be considered later.

Table Electron Constants

constant	*symbol*	*value* [*cgs*] [2]
charge	q	-4.8032×10^{-10}
mass	m	9.1094×10^{-28}
classical radius	R	2.82×10^{-13}
spin angular momentum	S	9.1329×10^{-28}
magnetic dipole moment	M	$-9.284764 \times 10^{-21}$
Planck's constant	h	6.6261×10^{-27}
speed of light	c	$2.99792458 \times 10^{10}$

2. Mass Inconsistency

2.1. Background

As discussed in [1], electron mass calculated from the spin angular momentum S using classical equations is more than 100 times greater than experimentally observed mass. To resolve the mass inconsistency, the classical model of the electron is shown to require a spin rotation speed much greater than the speed of light or a radius much greater than the classical radius. As shown in the following proposal, the mass inconsistency can be resolved without excessive rotation speeds or radii by introducing a negative mass into the electron model.

2.2. Negative Mass Proposal

Reference [1] addresses the inconsistency between the electron charge q and the charge derived from the spin magnetic moment M. The model for the electron resolved the inconsistency by introducing into the model a charge of polarity opposite to the polarity of q. Similarly, it is proposed in this article to introduce into the model a mass m^- having a negative mass to resolve the mass inconsistency.

The existence of negative mass is controversial. Numerous papers, for example [3], have been written which support the notion that there can be both positive and negative masses, just as there are positive and negative charges. The introduction of a negative mass into the electron model would certainly be helpful in resolving the mass inconsistency, discussed above.

An interesting property of negative mass is that the mass moves in a direction opposite to that of an applied force. From $F = ma$, a positive force F applied to

a negative mass m will cause a negative acceleration a. Therefore, negative mass will react to a positive force as if it were a negative force.

The core of the electron in the model is comprised of two parts:

- outer shell having a charge q^+ and a negative mass m^-
- central core having a charge q^- and a positive mass m^+

The distribution of q^- within the central core is unimportant as long as it appears to be located at the center of the outer shell.

The charge q of the electron is

$$q = q^+ + q^-$$

and the mass m of the electron is

$$m = m^+ + m^- .$$

Aside from its charge q^-, the nature of the central core was not discussed in [1]. It is proposed to have a positive mass m^+. The radius of the central core must be small enough such that its spin angular momentum is negligible compared with the spin angular momentum S of the outer shell. Spin angular momentum of a mass m at a radius r can be written as

$$S = \frac{2\pi m r^2}{T},$$

where T = period of rotation.

The masses m^- of the outer shell and m^+ of the central core have nearly the same absolute values. Therefore, if the radius r of the central core were to be $0.01R$, or 1% of the outer shell radius R, the spin angular momentum of the central core will be only 0.01% of the value for the outer shell and a negligible contributor to the total spin angular momentum S.

The negative mass m^- may be distributed along radials within the outer shell of the core, but appears to be located at a center of mass located in a ring of radius R_m to produce the spin angular momentum S. As will be seen below, the calculated value of R_m has a value close to but less than the predicted electron radius R_q. The outer ring spin angular momentum is

$$S = -\frac{2\pi m^- R_m^2}{T}.$$

The minus sign in the expression cancels the minus sign in the value for m^-, so S has a positive value. In [1], the spin was reversed to create a negative magnetic moment M from a spinning positive charge. That same reversal creates a positive spin angular momentum S from a spinning negative mass m^-.

Reference [1] assumes that the modeled electron is spinning less than but very close to the speed of light c. This assumption was made during the resolution of the charge inconsistency. Therefore,

$$T = \frac{2\pi R_q}{c},$$

where R_q is the electron radius to be calculated for the model.

$$S = -m^- \left(\frac{R_m^2}{R_q} \right) c$$

The rotation speed of the outer shell center of mass is

$$v = \frac{2\pi R_m}{T} = \left(\frac{R_m}{R_q} \right) c$$

The centrifugal force on m^- is

$$m^- \frac{v^2}{R_m} = m^- R_m \left(\frac{c}{R_q} \right)^2 .$$

The sign convention for forces in this article is: positive forces are repulsive and directed away from the center; negative forces are attractive and directed toward the center. The centrifugal force in this case is an attractive force because the mass m^- of the outer shell is negative.

3. Electric Forces

The electron modeled in [1] is a free electron, and the influence of external forces was not considered. The application of an external electric field will create forces on the two charges q^+ and q^- that tends to push them apart. Unless physically restrained, a displacement of q^- from the center of q^+ will result, creating an induced electric dipole moment. Reference [4] reports an experiment where the upper limit of the electric dipole moment was measured. If a dipole moment exists at all, it is very small, much smaller than the model in [1] with unrestrained charges would predict. Therefore, a fundamental assumption for the model proposed herein is that the electric dipole moment induced by an external electric field is zero.

Although the outer shell and central core of the model herein could be physically bound to each other, that is not a requirement. The two charges need not be physically constrained. Consequently, when an external electric field E is applied, these two components of the core must accelerate together at exactly the same rate to keep the core intact. Therefore, the accelerations are

$$\frac{qE}{m} = \frac{q^+ E}{m^-} = \frac{q^- E}{m^+}$$

The charge and mass relationships derived from the accelerations are

$$\frac{m^-}{m} = \frac{q^+}{q} \quad \text{and} \quad q^+ = \left(\frac{m^-}{m} \right) q$$

The mutually repulsive force upon each increment of q^+ due to all of the other increments of q^+ actually acts as a negative attractive force on the outer shell, because the mass of the shell is negative. The apparent force on all increments is

$$-\left(\frac{q^+}{r} \right)^2 = -\left(\frac{m^-}{m} \right)^2 \left(\frac{q}{r} \right)^2$$

where r is the radius of charge shell q^+. The attractive force between q^+ and q^- acts as a repulsive positive force upon the outer shell. The force is

$$-\left(\frac{q^+q^-}{r^2}\right)=-\left(\frac{m^-}{m}\right)\left(\frac{q-q^+}{r^2}\right)q=-\left(\frac{m^-}{m}\right)\left(\frac{q}{r}\right)^2\left[1-\left(\frac{m^-}{m}\right)\right].$$

The combined internal electrical forces act as a repulsive positive force on the outer shell:

$$-\left(\frac{m^-}{m}\right)\left(\frac{q}{r}\right)^2$$

4. Internal Forces

The sum of the internal forces must be zero for the core to be stable: The sum of the centrifugal and electrical forces is

$$m^-R_m\left(\frac{c}{r}\right)^2-\left(\frac{m^-}{m}\right)\left(\frac{q}{r}\right)^2=0$$

The solution for R_m in the above equation is the radius of the effective mass ring of the outer shell:

$$R_m=\left(\frac{q}{c}\right)^2\frac{1}{m}=2.82\times10^{-13}$$

R_m is exactly equal to the classical radius of the electron, calculated in [5]. The radius R_q of the charge ring is calculated in the following:

$$S=-m^-\left(\frac{R_m^2}{r}\right)c=-\left(\frac{m^-}{m}\right)\frac{q^4}{mc^3r},\quad r=-\left(\frac{m^-}{m}\right)\frac{q^4}{mc^3S}$$

The magnetic moment M for a spinning ring of charge q^+ and radius r is

$$M=\frac{q^+}{2}\omega r^2\ \text{[MKS] [6]}\quad M=\frac{q^+}{2c}\omega r^2\ \text{[cgs]}$$

where $\omega=\frac{2\pi}{T}$ and for the electron model, T = period of rotation = $\frac{2\pi}{c}r$. The magnet moment for the electron model is

$$M=-\frac{q^+}{2}r=-\frac{1}{2}\left(\frac{m^-}{m}\right)qr,\quad \left(\frac{m^-}{m}\right)=-\left(\frac{2M}{qr}\right)$$

(As explained in [1], the spin direction in the model is reversed such as to produce a negative spin magnet moment for a spinning positive charge.)

The radius R_q of the charge ring is the solution to

$$r=\left(\frac{2M}{qr}\right)\frac{q^4}{mc^3S}.$$

$$R_q=\sqrt{\frac{2M}{mS}\left(\frac{q}{c}\right)^3}=3.030\times10^{-13}=1.07R$$

The radius R_q of the charge ring is 7% greater than the radius R_m of the effective mass ring. R_q is considered to be the radius of the modeled electron.

The radius of the outer shell is stable. Since its mass is negative, any perturbation to the outer shell radius will cause the shell to react in the opposite direction, canceling out the perturbation. Also, the center of the outer shell is stable with respect to the inner core. A displacement of the center from the inner core center will increase the attractive force between the outer shell and inner core in a direction opposite to that of the displacement. The increase in attractive force on the negative mass of the outer shell will cause it to move such as to nullify the displacement and restore the net force on the outer shell to zero.

5. Internal Attributes

The two electron model radii, R_m and R_q, have been calculated for a ring-shaped core, so other attributes can now be calculated.

$$m^- = -\frac{2M}{qR_q}m = -1.162\times10^{-25} = -127.6m$$

$$m^+ = m - m^- = 1.171\times10^{-25} = 128.6m$$

$$q^+ = \left(\frac{m^-}{m}\right)q = 6.129\times10^{-8} = 127.6q$$

$$q^- = q - q^+ = -6.177\times10^{-8} = -128.6q$$

$$v = 0.93c$$

For a spherically-shaped core, R_m has the same value as for a ring-shaped core. However, the model for spin magnetic dipole moment M is different, and consequently the values for other attributes will be different also. The model for M is

$$M = \frac{q}{3}\omega r^2 \quad \text{[MKS] [7]} \quad M = \frac{q}{3c}\omega r^2 \quad \text{[cgs]}$$

The equations above for the ring-shaped core can be adjusted to those for a spherically-shaped core, by replacing "$2M$" with "$3M$". The internal attributes for a spherically-shaped core are then

$$R_q = \sqrt{\frac{3M}{mS}\left(\frac{q}{c}\right)^3} = 3.711\times10^{-13} = 1.32R$$

$$m^- = -\frac{3M}{qR_q}m = -1.424\times10^{-25} = -156.3m$$

$$m^+ = m - m^- = 1.433\times10^{-25} = 157.3m$$

$$q^+ = \left(\frac{m^-}{m}\right)q = 7.507\times10^{-8} = 156.3q$$

$$q^- = q - q^+ = -7.555\times10^{-8} = -157.3q$$

$$v = 0.76c\ .$$

6. Core Material

The model presented in [1] relied on an incompressible or compressible core

material to provide stability of the internal force balance. The model proposed herein does not for a ring-shaped core and for forces in the equatorial plane of a spherically-shaped core. However, for the later shape, core material is still required to provide a stable force balance along the spin axis, as detailed in [1].

7. Summary

A model of the electron has been proposed which has two opposite electrical charges and both positive and negative masses. The positive charge q^+ and negative mass m^- reside on the outer shell of the electron. The negative charge q^- and positive mass m^+ reside at the center of the electron. They have radii small enough so that the spinning negative charge does not significantly contribute to the net magnetic moment and the spinning positive mass does not significantly contribute to the spin angular momentum. The shape of the electron can be a ring, spherical, or a shape in between the two.

The intrinsic electric dipole moment of the modeled electron is zero. Also, there is no induced electric dipole moment when the electron is in an external electric field.

The internal attributes of the modeled electron are presented in the table below (Table 1). They are expressed as ratios to their corresponding external attributes.

The outer shell mass can be distributed along the radial direction. The mass can be thought of as being located along a circle having a radius equal to the "mass radius". The mass radius calculated for the electron model has a value exactly equal to the classical electron radius and independent of the core shape.

The charge radius is the radius of the positive charge on the surface of the outer shell. Its value is somewhat greater than the mass radius. The charge radius is considered to be the radius of the modeled electron. For a ring-shaped core, the calculated radius is only 7% greater than the classical radius.

The speed of the outer shell surface at the equator is assumed to be very close

Table 1. Internal/external attribute ratios.

attribute	*ring*	*sphere*
$\frac{\text{mass radius}}{\text{classical electron radius}}$	1.00	1.00
$\frac{\text{charge radius}}{\text{classical electron radius}}$	1.07	1.32
$\frac{\text{outer shell mass}}{\text{electron mass}} = \frac{\text{outer shell charge}}{\text{electron charge}}$	−127.6	−156.3
$\frac{\text{central core mass}}{\text{electron mass}} = \frac{\text{central core charge}}{\text{electron charge}}$	128.6	157.3
$\frac{\text{outer shell mass speed}}{\text{speed of light}}$	0.93	0.76

to the speed of light, and has been set equal to the speed of light in the calculations. The speed of the center of mass at the mass radius is somewhat less than the speed of light.

Single-charge single-mass models of the electron have a large inconsistency between the spin angular momentum S and the momentum calculated from spinning the electron mass at close to the speed of light. The proposed dual-charge dual-mass model eliminates this inconsistency with a radius very close to the classical radius and a rotation speed slightly less than the speed of light.

The single-charge electron model subjects the core to a very high tensile force. The net force on the negative-mass outer shell is zero, so there is no tensile force on the core. The outer shell is inherently stable, and for a ring-shaped core does not require any assumptions about the core material tensile strength or compressibility. There is no tensile force on the spherical core, but the compressive electrical force along the spin axis must still be physically balanced by the core material.

Conflicts of Interest

The author declares no conflicts of interest regarding the publication of this paper.

References

[1] Young, A. (2022) *Journal of Modern Physics*, **13**, 1117-1127. https://www.scirp.org/journal/paperinformation.aspx?paperid=118547 https://doi.org/10.4236/jmp.2022.137064

[2] Fischbeck, H.J. and Fischbeck, K.H. (1982) Formulas, Facts, and Constants: for Students and Professionals in Engineering, Chemistry and Physics. Springer, Berlin, Heidelberg. https://doi.org/10.1007/978-3-642-96681-1

[3] Paranjape, M.B. (2017) Don't Dismiss Negative Mass. Physics Today, 24 May. https://physicstoday.scitation.org/do/10.1063/pt.6.3.20170524a/full/

[4] ACME Collaboration (2018) *Nature,* **562**, 355-360. https://doi.org/10.1038/s41586-018-0599-8

[5] Haken, H., Wolf, H.C. and Brewer, W.D. (2005) The Physics of Atoms and Quanta. In: *Advanced Texts in Physics*, Springer, Berlin, Heidelberg, p. 69. https://link.springer.com/chapter/10.1007/3-540-29281-0_6 https://doi.org/10.1007/3-540-29281-0

[6] Halliday, D., Resnick, R. and Krane, K.S. (2010) *Physics*, **2**, 819.

[7] Arora, C.L. (2010) Refresher Course in B.Sc. Physics. Vol. 1, S. Chand Publishing, New Delhi, p. 406.

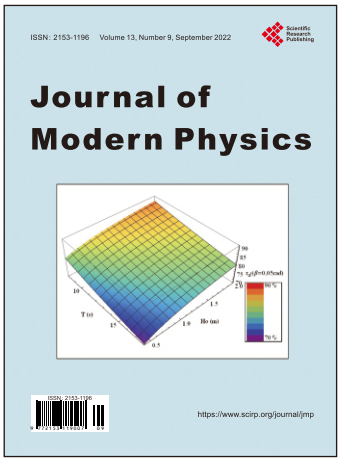

Call for Papers

Journal of Modern Physics

ISSN: 2153-1196 (Print) ISSN: 2153-120X (Online)
https://www.scirp.org/journal/jmp

Journal of Modern Physics **(JMP)** is an international journal dedicated to the latest advancement of modern physics. The goal of this journal is to provide a platform for scientists and academicians all over the world to promote, share, and discuss various new issues and developments in different areas of modern physics.

Editor-in-Chief

Prof. Yang-Hui He City University, UK

Subject Coverage

Journal of Modern Physics publishes original papers including but not limited to the following fields:

Biophysics and Medical Physics
Complex Systems Physics
Computational Physics
Condensed Matter Physics
Cosmology and Early Universe
Earth and Planetary Sciences
General Relativity
High Energy Astrophysics
High Energy/Accelerator Physics
Instrumentation and Measurement
Interdisciplinary Physics
Materials Sciences and Technology
Mathematical Physics
Mechanical Response of Solids and Structures
New Materials: Micro and Nano-Mechanics and Homogeneization
Non-Equilibrium Thermodynamics and Statistical Mechanics
Nuclear Science and Engineering
Optics
Physics of Nanostructures
Plasma Physics
Quantum Mechanical Developments
Quantum Theory
Relativistic Astrophysics
String Theory
Superconducting Physics
Theoretical High Energy Physics
Thermology

We are also interested in: 1) Short Reports—2-5 page papers where an author can either present an idea with theoretical background but has not yet completed the research needed for a complete paper or preliminary data; 2) Book Reviews—Comments and critiques.

Notes for Intending Authors

Submitted papers should not have been previously published nor be currently under consideration for publication elsewhere. Paper submission will be handled electronically through the website. All papers are refereed through a peer review process. For more details about the submissions, please access the website.

Website and E-Mail

https://www.scirp.org/journal/jmp **E-mail: jmp@scirp.org**

What is SCIRP?

Scientific Research Publishing (SCIRP) is one of the largest Open Access journal publishers. It is currently publishing more than 200 open access, online, peer-reviewed journals covering a wide range of academic disciplines. SCIRP serves the worldwide academic communities and contributes to the progress and application of science with its publication.

What is Open Access?

All original research papers published by SCIRP are made freely and permanently accessible online immediately upon publication. To be able to provide open access journals, SCIRP defrays operation costs from authors and subscription charges only for its printed version. Open access publishing allows an immediate, worldwide, barrier-free, open access to the full text of research papers, which is in the best interests of the scientific community.

- High visibility for maximum global exposure with open access publishing model
- Rigorous peer review of research papers
- Prompt faster publication with less cost
- Guaranteed targeted, multidisciplinary audience

Scientific Research Publishing

Website: https://www.scirp.org

Subscription: sub@scirp.org

Advertisement: service@scirp.org